

Promoting intermediates transformation by boosting H₂O dissociation over core-shell Pd@CoO Janus for acetone efficacious oxidation

Yani Wu ^{a,1}, Yadi Wang ^{a,1}, Jicheng Liu ^{a,1}, Zeyu Jiang ^{a,*}, Jialei Wan ^a, Jingjing Wang ^a, Shouning Chai ^a, Chunli Ai ^a, Fan Dang ^a, Reem Albilali ^b, Chi He ^{a,c,**}

^a Department of Environmental Science and Engineering, Xi'an Jiaotong University, Xi'an, Shaanxi 710049, PR China

^b Department of Chemistry, College of Science, Imam Abdulrahman Bin Faisal University, P.O. Box 1982, Dammam 31441, Saudi Arabia

^c National Engineering Laboratory for VOCs Pollution Control Material & Technology, University of Chinese Academy of Sciences, Beijing 101408, PR China



ARTICLE INFO

Keywords:

Acetone
Catalytic oxidation
Core-shell Pd@CoO Janus
H₂O dissociation
Aldehyde intermediate transformation

ABSTRACT

Reactivity loss by intermediates aggregation and water vapor inhibition are two major and longstanding challenges for the noble-metal-based catalysts in oxygenated volatile organic compounds (OVOCs) oxidation. Herein, the core-shell Pd@CoO Janus sites are creatively designed and stabilized over the HSAPo-34 support. Quasi *in situ* XPS spectra reveal that the strong interactions in Pd@CoO Janus sites promote the charge redistribution and electron back-donation through Pd-O-Co coordination. Therefore, abundant positively charged Pd²⁺ sites are formed and oxygen species transformation is facilitated, which significantly promote the low-temperature efficiency of acetone oxidation. Furthermore, the Pd@CoO/HSAPo-34 catalyst facilitates H₂O molecules dissociation and produce reactive OH_{Ter} and OH_{Tri} species, which considerably promotes the rapid decomposition of aldehyde intermediate via attacked CH₂O^{*} group, ensuring low-temperature oxidation of acetone. This work provides valuable guidance to develop specific catalysts with functional active sites for rationally utilizing H₂O molecules to improve low-temperature performance and modulate reaction pathways during OVOCs oxidation.

1. Introduction

Volatile organic compounds (VOCs) pose a significant hazard to human health and the environment. Therefore, the development of promising technologies to eliminate the industrial emission of VOCs is one of the biggest challenges facing the chemical industry in the 21st century [1–3]. Amongst, acetone (C₃H₆O) is mostly concerned attributing to its great proclivity to create ozone and substantial discharged from vast industrial processes such as pharmaceutical and package printing [4]. The catalytic oxidation is recognized as one of the most efficient VOCs removal technology attributing to its economic viability, high efficiency, and harmless products (CO₂ and H₂O) [5–7]. The core of this strategy is designing and developing efficient catalysts. The noble-metal-based catalysts have attracted broad interests for VOCs decomposition attributing to their superb low-temperature catalytic performance [8–10]. Amongst, the supported Pd-based catalysts are mostly concerned attributing to their relatively low price and high

reactivity [11–13]. Specifically, the Pd-based catalysts are dominated for the catalytic oxidation of OVOCs. One such example given by Zhao and co-workers demonstrated that Pd-based catalysts exhibit enhanced activity in the oxidation of acetone due to the presence of a substantial quantity of oxygen species [14]. Another study by Yue et al. reported that the Pd-based catalysts with adjustable metal state can significantly facilitate the methyl-ethyl-ketone oxidation process [15].

The progress has been made, while the challenge surrounding for improving the stability of Pd-based catalysts is remaining. From industrial reality, water vapor is a generally existed component in industrial OVOCs-contained exhausts, which usually obviously inhibits the catalytic oxidation efficiency of OVOCs owing to the competitive adsorption or the poisoning effect over the active sites, resulting in the decreased reactivity [16]. For instance, our previous work found that the methyl-ethyl-ketone oxidation efficiency over Pt/K-(Al)SiO₂ catalyst decreased by 4–15 % when 3 vol% H₂O was introduced into the reaction system [17]. Another similar phenomenon can also be determined that

* Corresponding author.

** Corresponding author at: Department of Environmental Science and Engineering, Xi'an Jiaotong University, Xi'an, Shaanxi 710049, PR China.

E-mail addresses: jiangzeyu@xjtu.edu.cn (Z. Jiang), chi_he@xjtu.edu.cn (C. He).

¹ These authors contributed equally to this work.

around 32.0 % and 27.7 % loss in methyl-ethyl-ketone conversion over $\text{Pt}_{0.3}/\text{SiO}_2$ and $\text{Pt}_{0.3}\text{Mn}_5/\text{SiO}_2$ after introducing H_2O at 180 °C [18]. Furthermore, the water vapor would cover the active sites and inevitably weaken the oxidation capacity of the catalysts, giving rise to restrained activity and incomplete oxidation intermediates. Hence, the development of effective strategies aiming at enhancing the water vapor resistance of noble-metal-based catalysts is crucial and dependable for the efficient catalytic oxidation of OVOCs.

The usual strategy for improving the water vapor resistance is preventing the competitive adsorption over catalyst surface [19]. For instance, Xiao et al. demonstrated that water vapor resistance could be strengthened by preventing the adsorption of H_2O molecules through the doping of Ni species and the effective modification of electronic and chemical properties of Pt sites [20]. Additionally, activating H_2O molecules into other reactive species, such as -OH and -HOH groups, is seen as another effective strategy for improve the water vapor resistance of catalysts. For instance, our previous studies reported that H_2O molecules can be activated on the catalyst surface and participate in the catalytic reactions. We proposed that the introducing of low content water vapor (< 1 vol%) slightly promotes the activity of $\text{Mn}/\text{Al}_2\text{O}_3/\text{COR}$ catalyst for ethyl acetate oxidation [21]. This enhancement is attributed to the positive effect of generated -OH groups obtained from the dissociation of H_2O , which outweighs the inhibition of water vapor [21]. Deng et al. showed that the -OH groups derived from H_2O dissociation can activate lattice oxygen atoms and enhance the efficiency of catalysts [22]. Zhang et al. proposed that H_2O molecules stabilized by oxygen vacancies of MnCeO_x can provide -HOH active sites that improved the adsorption capacities of oxygen, toluene, and benzaldehyde species, which in-turn enhanced the toluene oxidation [23]. Another similar investigation was also provided by Ma and co-workers [24]. Therefore, it is reasonable to predict that the accelerated dissociation of H_2O molecules should be a potential and promising strategy for OVOCs oxidation under humid conditions.

The core of this strategy is modulating the electronic structure of active sites to optimize the adsorption and activation processes of H_2O molecules over the catalysts surface. Generally, the H_2O dissociation on the catalyst surface is usually induced by the electron transformation from the active component to H_2O molecules through chemical bond interaction [25,26]. To our knowledge, these previous studies mainly focus on the effect of different active components and ratios on the activation of H_2O , but the relationship of H_2O dissociation with chemical bond interaction has not been fully explored. Notably, the interactions between Pd and transition metal oxides (MO_x) can facilitate the formation of $\text{Pd}^{\delta+}$ sites through their coupling p-d orbits electronic transfer. The chemical bond interactions through Pd-O-M coordination can be further promoted by the specific core-shell Janus structures. For example, Li and co-workers revealed that the metal-support electronic interactions occurred at $\text{Pd}-\text{CeO}_2$ interfaces, and PdO_2 is transformed into a hydroperoxyl PdOOH species via proton transfer over the $\text{Pd}-\text{CeO}_2$ catalyst [27]. As one of the typical transition metal oxides, CoO species is more intended to accelerate the cleavage of H_2O molecules and the mobility of surface hydroxyl group due to its high redox-oxide efficiency and abundant variable valence states [28,29]. Jiang et al. reported that the unsaturated-coordination Co atoms can facilitate the dissociation of H_2O molecules and the activation of lattice oxygens for toluene oxidation [30]. Hence, it is of great significance to design the $\text{Pd}@\text{CoO}$ core-shell Janus active sites for promoting the dissociation and activation of low concentration H_2O molecules, so as to improve the water resistance and catalytic efficiency.

Herein, the $\text{Pd}@\text{CoO}/\text{HSAPO-34}$ catalyst containing core-shell Janus sites with tailored local coordination structures and electronic states was designed and synthesized through a two-step thermal-depolymerization method. This prepared $\text{Pd}@\text{CoO}/\text{HSAPO-34}$ catalyst exhibits the outstanding efficiency for the catalytic oxidation of acetone, over which 500 ppm of acetone can be fully oxidized at 240 °C with a GHSV of 75,030 $\text{mL}\cdot\text{g}^{-1}\cdot\text{h}^{-1}$. The determined structure-activity relationships

reveal that the interactions between Pd sites and CoO shell promote the charge redistribution and electron back-donation through Pd-O-Co coordination, which significantly promotes the low-temperature efficiency of acetone oxidation. Importantly, the core-shell $\text{Pd}@\text{CoO}$ can greatly facilitate the dissociation of H_2O molecules to active surface -OH groups. The generated reactive OH_{Ter} and OH_{Tri} species (hydrogenated O_{latt}) can significantly promote the rapid conversion of aldehyde by-products via attacked the CH_2O^* group, which in-turn promotes the acetone being fully oxidized at low-temperatures. This study contributes to the establishment of a foundational comprehension about the pivotal significance of low concentrations of H_2O molecules during catalytic oxidation of OVOCs. This newfound knowledge will serve as valuable guidance for researchers in their efforts to develop specific catalysts with functional active sites for the reasonable utilization of activated H_2O molecules to enhance the low-temperature performance and modulate the reaction pathways.

2. Experimental section

2.1. Catalyst preparation

The Pd nanoparticles (NPs) were prepared via a thermal reduction procedure. Typically, 0.25 mmol of $\text{Pd}(\text{acac})_2$ was dissolved in 50 mL of oleyl amine solution under vigorous stirring at 70 °C for 10 min. The obtained solution was transferred into high temperature autoclave and then heated from 70 to 180 °C for 40 min under 0.1 MPa of CO atmosphere (40 $\text{mL}\cdot\text{min}^{-1}$). The mixed solution was then separated through centrifugation and washed with ethanol and ethanol-cyclohexane (3: 1) thoroughly. Following, the collected Pd NPs powder was dried naturally. The as-prepared Pd NPs were dispersed in 60 mL oleylamine solution under stirring at 45 °C for 45 min and then cooled down to the room temperature. The resulting solution was mixed with 0.015 g $\text{Co}(\text{acac})_2$ and stirred at 70 °C until the solution is transparent, which was transferred into autoclave and then heated from 70 to 240 °C for 1 h under N_2 atmosphere (40 $\text{mL}\cdot\text{min}^{-1}$). The $\text{Pd}@\text{CoO}$ Janus were finally collected by centrifugation and washed with ethanol and ethanol-cyclohexane mixture.

To prepare the $\text{Pd}/\text{HSAPO-34}$ and $\text{Pd}@\text{CoO}/\text{HSAPO-34}$ catalysts, a certain amount of HSAPO-34 was dispersed in deionized water, which was mixed with 0.2 g cetyltrimethyl ammonium bromide (CTAB) and 5 g tetrapropylammonium hydroxide (TPAOH). Then the desirable amount of as-prepared Pd and $\text{Pd}@\text{CoO}$ nanoparticles dispersed in N,N -dimethylformamide (DMF) solution was injected dropwise into above solution under vigorous stirring. After that, the mixture was stirred at 60 °C for 12 h. The excess solution was evaporated from the mixture by rotary evaporator under vacuum. After drying at 60 °C overnight, the collected powder was calcined at 350 °C for 3 h in air and reduced in 5 % v/v H_2/Ar stream for 2 h at 300 °C (heating rate of 5 °C•min⁻¹), and the obtained catalysts were denoted as $\text{Pd}/\text{HSAPO-34}$ and $\text{Pd}@\text{CoO}/\text{HSAPO-34}$, respectively.

2.2. Characterizations

The high-resolution transmission electron microscopy (HR-TEM) and EDX-mapping images were recorded over a Talos F200X (Thermo Scientific, U.S.) microscope at 300 kV. The X-ray diffractions (XRD) were recorded on LabX XRD-6100 diffractometer (Cu K_α radiation equipped with $\lambda = 1.54178 \text{ \AA}$; 45 kV; 40 mA). N_2 adsorption-desorption curves were measured at 77 K on a Builder SSA-6000 apparatus. X-ray photo-electron spectroscopic (XPS) data were collected from an ESCALAB Xi⁺ instrument (Thermo Scientific K-Alpha, U.S.) with Al-K radiation ($h = 1253.6 \text{ eV}$) and analyzed by Advantage software. Fourier transform infrared spectra (FT-IR) were recorded on Tensor II (Bruker, Germany) at a resolution of 4 cm^{-1} with 32 scans at room temperature. The temperature-programmed reduction/desorption experiments ($\text{H}_2\text{-TPR}$; $\text{NH}_3/\text{O}_2/\text{CO}/\text{H}_2\text{O-TPD}$) were conducted on the chemisorption analyzer

(Builder, China) containing a TCD detector. The thermogravimetric-differential thermal analysis (TG-DTA) were performed using a thermogravimetric analyzer (DTA-60, Shimadzu, Japan). Quasi *in situ* XPS experiments were conducted over a Thermo esca-lab 250Xi⁺ (Thermo fisher, America) instrument. The proton transfer reaction-mass reaction (PTR-QMS) were carried out on PTR Drift Tube (IonSniffer Q300, Austria), protonated water (H_3O^+) is used as a reagent to ionize the VOCs of interest. *In situ* diffuse reflectance infrared Fourier transform spectroscopy (*In situ* DRIFTS) of NH_3 , CO, acetone, and H_2O adsorption were recorded at a resolution of 4 cm^{-1} with 100 scans in the range of $600\text{--}4000 \text{ cm}^{-1}$ on the Tensor 37 (Bruker, Germany) infrared spectrometer containing an MCT detector. The procedures of all these characterizations are detailed in [Supporting Information](#).

2.3. Catalytic performance evaluation

The performance of prepared catalysts for the catalytic oxidation of acetone was investigated in a continuous flow fixed bed reactor equipped with a quartz tube (10 mm, diameter) at atmospheric pressure. In each test, 0.2 g of catalyst (40–60 mesh) was fixed in the quartz tube. All gas flow rates were controlled by mass flow meters. 500 ppm acetone feed gas was generated in a constant temperature water bath at 25°C with an N_2 bubbler mixed with air. The total flow rate was set as $250 \text{ mL}\cdot\text{min}^{-1}$ to maintain the gas hourly space velocity of $75,030 \text{ mL}\cdot\text{g}^{-1}\cdot\text{h}^{-1}$. The catalyst bed was then brought to the desired temperature controlled by a K-type thermocouple, and allowed to equilibrate for 30 min before on-line sampling operating. The concentration of acetone and CO_2 was measured using an on-line gas chromatograph (GC-9890B; Linghua, China) equipped with a flame

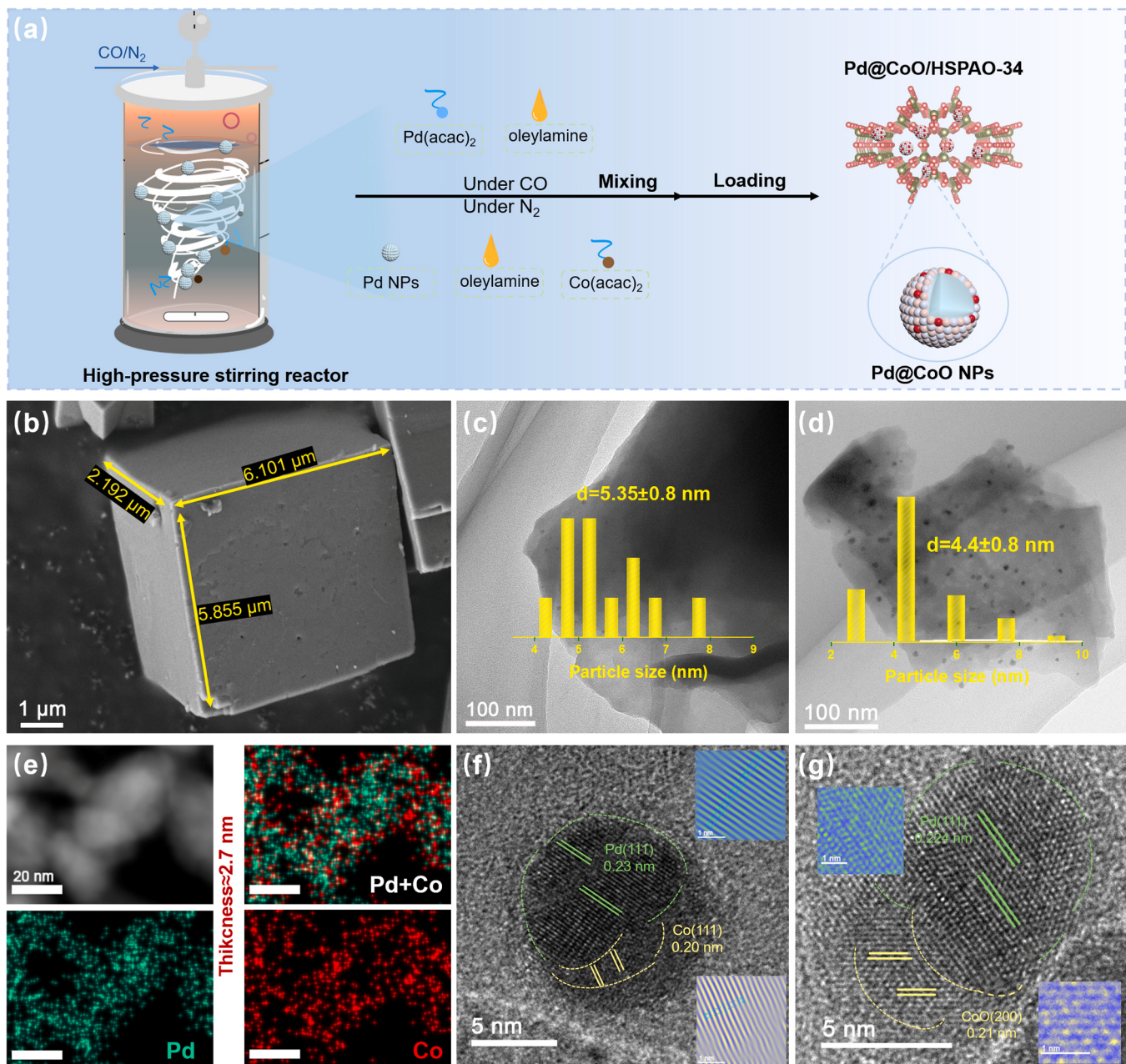


Fig. 1. (a) A described preparation procedures for the synthesis of Pd@CoO/HSAPO-34 catalyst, (b) SEM image of HSAPO-34 support, and TEM images and corresponding Pd distributions of (c) Pd/HSAPO-34 and (d) Pd@CoO/HSAPO-34 catalysts; (e) HAADF-STEM image and EDX-mapping images of Pd@CoO Janus shells; (f,g) HR-TEM images of Pd@CoO/HSAPO-34 catalyst.

ionization detector (FID). The detailed methods for evaluating the catalytic performance are provided in [Supporting Information](#).

2.4. Theoretical investigation

The first-principles were used to perform all density functional theory (DFT) calculations within the generalized gradient approximation (GGA) using the Perdew-Burke-Ernzerhof (PBE) formulation. The projected augmented wave (PAW) potentials were adopted to describe the ionic cores and take valence electrons into account using a plane wave basis set with a kinetic energy cutoff of 520 eV. Partial occupancies of the Kohn-Sham orbitals were allowed using the Gaussian smearing method and a width of 0.05 eV. The electronic energy was considered self-consistent when the energy change was smaller than 10^{-4} eV. A geometry optimization was considered convergent when the energy change was smaller than $0.05 \text{ eV}\cdot\text{\AA}^{-1}$. In our structure, the U correction is used for Pd and Co atoms. The vacuum spacing in a direction perpendicular to the plane of the structure is 20 Å for the surfaces. The Brillouin zone integration is performed using $1 \times 1 \times 1$ Monkhorst-Pack k -point sampling for a structure. Finally, the adsorption energies (E_{ads}) were calculated as Eq. (1),

$$E_{\text{ads}} = E_{\text{ad/sub}} - E_{\text{ad}} - E_{\text{sub}} \quad (1)$$

where $E_{\text{ad/sub}}$, E_{ad} , and E_{sub} are the total energies of the optimized adsorbate/substrate system, the adsorbate in the structure, and the clean substrate, respectively.

3. Results and discussion

3.1. Physical and chemical properties

In this work, a one-step thermal reduction method was employed for the synthesis of Pd nanoparticles, which were further coated with a CoO shell through a high-pressure ligand depolymerization, and Pd-O-Co coordination was formed via a further calcination process (Fig. 1a, Figs. S1 and S2). Following, the synthesized core-shell Pd@CoO Janus was stabilized on the HSAPO-34 support. The morphology of typical catalysts was explored from the FE-SEM and HR-TEM images, and the representative patterns are exhibited in Fig. 1. From Fig. 1b, the HSAPO-34 support presents typical nano-cubic shapes with the crystal size around 5–6 μm. After anchoring the Pd/Pd@CoO active sites, the HR-TEM images (Fig. 1c and 1d) reveal that the formation of the flake assembled structures with about 800 nm in diameter for the Pd/HSAPO-34 and Pd@CoO/HSAPO-34 catalysts. The Pd nanoparticles with around 5.35 ± 0.8 nm are dispersed on HSAPO-34 support for the Pd/HSAPO-34 catalyst (Fig. 1c). Comparatively, the particle size distribution of Pd@CoO Janus is determined as 4.4 ± 0.8 nm (Fig. 1d).

The high-angle annular dark field scanning transmission electron microscopy (HAADF-STEM) image (Fig. 1e and S3) further confirms the existence of Pd@CoO Janus structure, in which the thickness of the CoO layer is merely around 2.7 nm. EDX-mapping images of Pd@CoO/HSAPO-34 catalyst provides direct evidence for the CoO layer on the surface of Pd NPs by the obviously larger element signal distribution of Co compared with Pd. The interplanar spacings of Pd (111) with around 0.22–0.23 and CoO (200) with 0.20–0.21 nm are determined (Fig. 1f, 1g, and S3), indicating that doped Co species can be easily transferred to the surface and then the Pd-CoO Janus will be constructed [31]. The CO-TPD experiment provides further evidence in Table S1, showing that

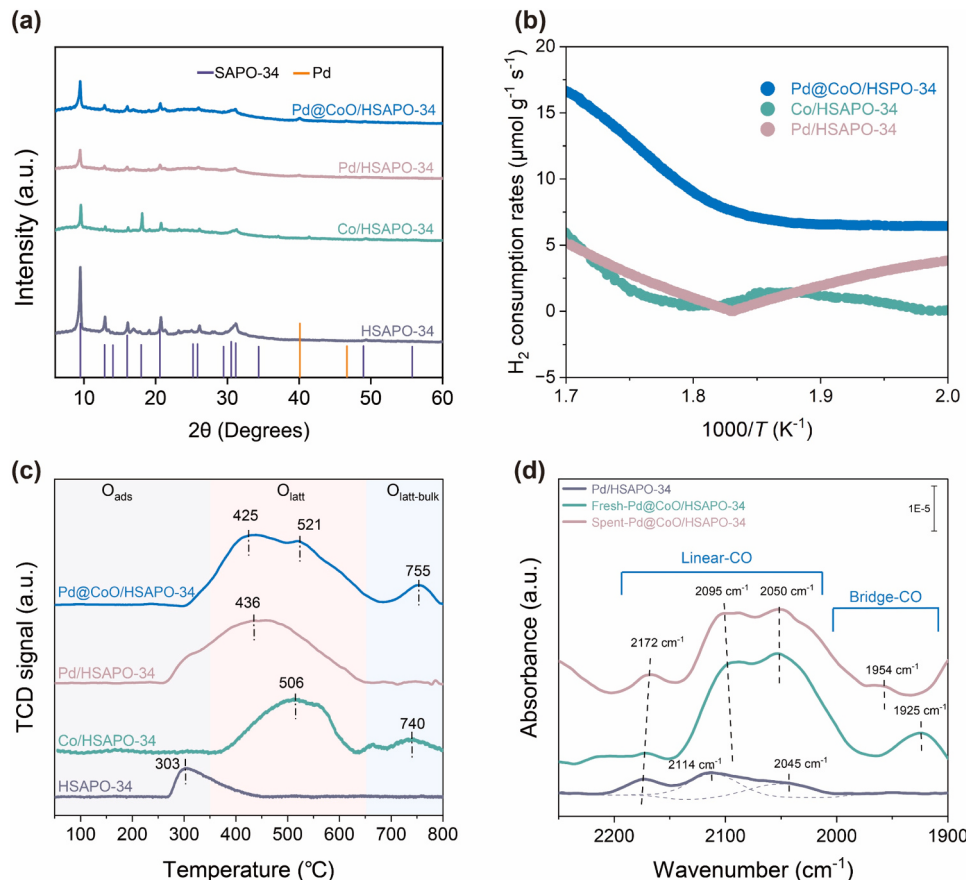


Fig. 2. (a) XRD patterns, (b) Initial H_2 consumption rates, (c) O_2 -TPD profiles, and (d) DRIFTS of CO adsorption for the prepared catalysts.

the Pd dispersion over Pd/HSAPO-34 and Pd@CoO/HSAPO-34 catalysts are determined as 77.8 % and 79.8 %, respectively. The CoO shell promotes fine Pd NPs dispersion and prevents their aggregation during the calcination process [32].

Wide-angle XRD patterns of the synthesized catalysts are given in Fig. 2a. The diffractograms at $2\theta = 9.5^\circ, 13.0^\circ, 15.0^\circ, 20.9^\circ$, and 31.0° are corresponding to the chabazite (CHA) framework of HSAPO-34 (JCPDS #47-0429) [33,34]. Notably, the catalysts obtained by weak-alkali treatment exhibit equivalent peak as the pure HSAPO-34 support, which demonstrates that the addition of TPAOH and CTAB poses a negligible effect on the crystallization of HSAPO-34 support with well-ordered pore structure. The peak at $2\theta = 40.1^\circ$ observed in diffraction patterns of all supported-Pd catalysts is assigned to the (111) plane of Pd species (JCPDS #46-1043) [35]. The characteristic peaks related to CoO species cannot be detected attributing to its low content. The specific surface area (S_{BET}) and pore size distribution of prepared catalysts were determined by N_2 sorption isotherms (Fig. S4 and Table S1). The detected sharp increase at $P/P_0 < 0.1$ in adsorption isotherms is associated with the filling of micropores, related to the CHA framework of HSAPO-34 support. All catalysts exhibit the classical type IV adsorption isotherms with an obvious hysteresis loop at P/P_0 of 0.4–0.8, suggesting that these catalysts possess well-ordered mesoporous and narrow pore size distributions [36]. These results indicate that the doping of active sites affects the original microporous structure of HSAPO-34, while posing a negligible effect on its crystallization. The S_{BET} and the pore volume (Table S1) of supported catalysts have a slight decline compared with HSAPO-34 support, ascribing to the block of pores and structure collapse during the doping of nanoparticles in subsequent preparation processes [7,37,38]. Comparatively, the S_{BET} and pore volume of Pd@CoO/HSAPO-34 ($224.5 \text{ m}^2 \cdot \text{g}^{-1}$; $0.24 \text{ cm}^3 \cdot \text{g}^{-1}$) are much larger than Pd/HSAPO-34 ($121.9 \text{ m}^2 \cdot \text{g}^{-1}$; $0.17 \text{ cm}^3 \cdot \text{g}^{-1}$), attributing to the higher dispersion of Pd@CoO nanoparticles.

The FT-IR spectra of HSAPO-34, Co/HSAPO-34, Pd/HSAPO-34, and Pd@CoO/HSAPO-34 (fresh and spent) catalysts are displayed in Fig. S5. The band at $478, 645, 724$ and 1100 cm^{-1} can be assigned to the SiO_4 structure, double 6-ring (D6R), asymmetric and symmetric O–P–O stretches in HSAPO-34 framework, respectively [33]. All catalysts exhibit a broad and intensive absorption peak at around $3300\text{--}3600 \text{ cm}^{-1}$, which can be attributed to the stretching and bending vibrations of surface hydroxyls and/or adsorbed H_2O molecules. The vibratory mode bonding of the physical absorbed H_2O molecule on catalysts is also specified with the peaks at 1648 cm^{-1} . Notably, the relative content of surface hydroxyls groups is reduced for the spent Pd@CoO/HSAPO-34 catalyst, indicating the consumption of surface hydroxyls groups during acetone oxidation.

Following, the reactive oxygen mobility and catalyst reducibility were explored by $\text{H}_2\text{-TPR}$ (Fig. 2b and Fig. S6) and $\text{O}_2\text{-TPD}$ (Fig. 2c) profiles. As shown in Fig. S6, the peaks below 400°C can be attributed to the reduction of Co^{3+} to Co^{2+} , whereas the peaks centered at $500\text{--}600^\circ\text{C}$ are associated with the reduction of Co^{2+} to Co^0 [39]. Additionally, another reduction peak in the range of $200\text{--}300^\circ\text{C}$ can also be detected, which can be assigned to the reduction of surface oxygen species from Pd@CoO Janus (Pd-O-Co) [40]. Significantly, the reduction temperature of $\text{Co}^{\delta+}$ species from Pd@CoO/HSAPO-34 catalyst is much lower than that of other catalysts. This phenomenon can be ascribed to that the strong interactions between Pd species and CoO shell promote the charge redistribution and electron back-donation through the Pd-O-Co coordination, and in-turn improve the reducibility of core-shell Pd@CoO Janus active sites. The quantitative initial H_2 consumption rate (H_c) of these prepared catalysts ($200\text{--}300^\circ\text{C}$) is given in Fig. 2b. Notably, the H_c of adsorbed oxygen species over Pd@CoO/HSAPO-34 ($12.64 \mu\text{mol} \cdot \text{g}^{-1} \cdot \text{s}^{-1}$) surpasses that of Pd/HSAPO-34 ($2.47 \mu\text{mol} \cdot \text{g}^{-1} \cdot \text{s}^{-1}$) and Co/HSAPO-34 ($1.45 \mu\text{mol} \cdot \text{g}^{-1} \cdot \text{s}^{-1}$) catalysts, suggesting that the Pd@CoO/HSAPO-34 catalyst possesses the superb low-temperature reducibility [41].

$\text{O}_2\text{-TPD}$ profiles were further provided to evaluate the mobility of

oxygen species for these catalysts. As shown in Fig. 2c, the desorption peaks centered at $425, 436$, and 506°C over the Pd@CoO/HSAPO-34, Pd/HSAPO-34, and Co/HSAPO-34 catalysts are assigned to the surface lattice oxygen (surface $\text{O}_{\text{latt}}, \text{O}^{2-}$) [42,43]. The peaks at 765 and 740°C contribute to the desorption of bulk lattice oxygen species (bulk $\text{O}_{\text{latt}}, \text{O}^{2-}$) [44]. The $\text{O}_2\text{-TPD}$ profiles reveal that the activation and transformation of O_{latt} species are greatly enhanced for the Pd@CoO/HSAPO-34 catalyst owing to the weakened Co-O bonding strength from Pd@CoO Janus structure. Additionally, the dependence of active oxygen species and acetone dissociation on catalyst surface was further explored by acetone-TPSR-MS (Fig. S7).

As demonstrated in Fig. 2d, with regard to the peaks at 2172 and 2114 cm^{-1} (attributed to the adsorbed CO), the linearly-bonded CO adsorption peak located at 2050 and 2095 cm^{-1} can be detected for the fresh and spent Pd@CoO/HSAPO-34 catalysts, and the corresponding peak over Pd/HSAPO-34 catalyst is centered at around 2045 cm^{-1} . A broad band existing in the range of $1840\text{--}2000 \text{ cm}^{-1}$ is ascribed to the bridged and/or three-hollowed CO adsorption on Pd nanoparticles. It is demonstrated that a shift to the higher frequency (from 2045 to $2050\text{--}2095 \text{ cm}^{-1}$) is probably associated with the weaker electron back-donation from Pd atoms to the antibonding π^* orbital of the linearly coordinated CO molecule (the low electron density of surface Pd on support), attributing to the presence of tiny Pd nanoparticles [7]. This phenomenon is in accordance with the results of HR-TEM images that the highly dispersed Pd@CoO Janus sites are determined (Figs. 1c and 1d).

3.2. Surface electronic properties

Understanding the electronic structure and elemental state is crucial, which is fundamental for establishing the structure-activity relationships. Firstly, X-ray photoelectron spectra (XPS) were analyzed to determine the state of Pd, Co, and O species on the surface of catalysts. By using the curve-fitting approach, the Pd 3d XPS spectra of fresh catalysts are displayed in Fig. 3a. Apparently, two distinct states of Pd species for Pd/HSAPO-34 and Pd@CoO/HSAPO-34 catalysts can be assigned to the Pd^0 and Pd^{2+} species, respectively. The peaks at $335.3\text{--}335.7$ and $339.5\text{--}340.9 \text{ eV}$ are ascribed to the metallic Pd species [45], and peaks at 337.7 and $341.5\text{--}342.6 \text{ eV}$ are attributed to the oxidized Pd species [46]. Notably, the proportion of positively charged Pd^{2+} species increases from 47.3 % of Pd/HSAPO-34 catalyst to 51.1 % of Pd@CoO/HSAPO-34 catalyst (Table S2). Moreover, the positive shift of the Pd 3d peak is determined as 0.4 eV. These results suggest the electron donation from Pd atoms to CoO through the generated Pd-O-Co coordination in Pd@CoO/HSAPO-34 catalyst. Fig. 3b shows the Co 2p XPS spectra of prepared catalysts. The exhibited two main peaks are attributed to the $\text{Co } 2p_{3/2}$ (797.4 eV) and $\text{Co } 2p_{1/2}$ (782.2 eV) orbital [47]. The separation by 15.2 eV is attributed to the spin-orbit splitting of $\text{Co } 2p_{1/2}$ and $\text{Co } 2p_{3/2}$, in agreement with the values reported in the literature [48]. The deconvolution of $\text{Co } 2p_{3/2}$ contains peaks at 779.6 and 782.2 eV , which can be assigned to Co^{3+} and Co^{2+} species, respectively. The peaks at 794.0 and 797.4 eV are ascribed to the spin-orbit characteristics of $\text{Co } 2p_{1/2}$ [49]. The proportion of Co^{2+} species increases from 51.7 % of Co/HSAPO-34 catalyst to 62.8 % of Pd@CoO/HSAPO-34 catalyst (Table S3). The higher proportion of Co^{2+} species present in the Pd@CoO/HSAPO-34 catalyst can also be ascribed to the strengthened electron back donation from Pd sites, in accordance with the changes of the valence state of Pd species.

The surface oxygen species were further evaluated using O 1 s XPS spectra (Fig. 3d). The peaks at $529.5\text{--}529.9 \text{ eV}$ can be assigned to the saturated lattice oxygens (denoted as O_{latt}), while the peaks at $530.0\text{--}531.5 \text{ eV}$ are attributed to the active surface adsorbed oxygens (denoted as O_{ads}) [50,51]. The O_{ads} peaks can be associated with surface chemisorbed oxygen and hydroxyl species [52]. Furthermore, the proportion of the peaks attributed to O_{ads} and O_{latt} species in each catalyst was subsequently quantified and provided in Fig. 3d. Obviously, the

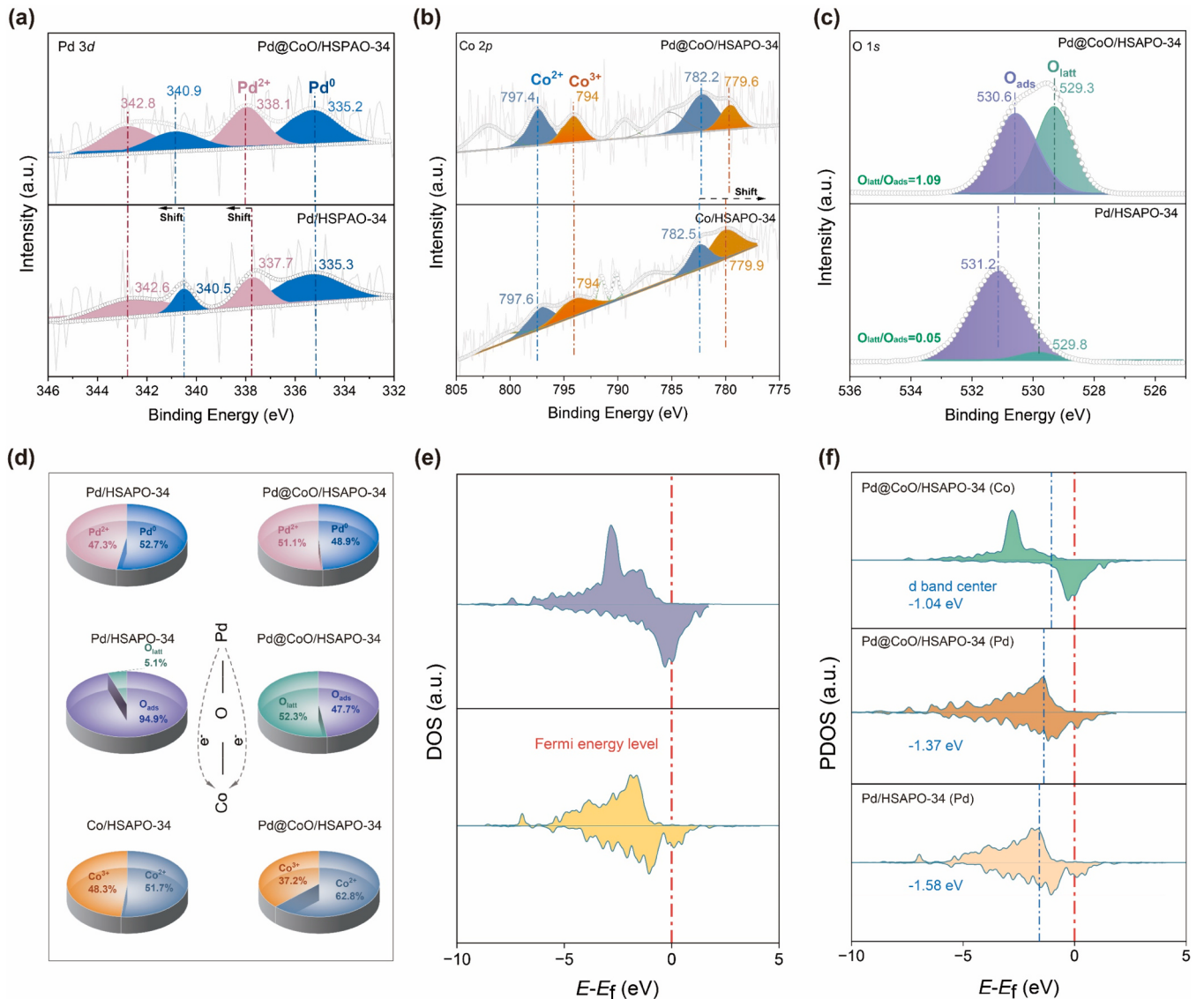


Fig. 3. (a) Pd 3d, (b) Co 2p, and (c) O 1 s XPS spectra of prepared catalysts; (d) Determined Pd, O, and Co ratio of prepared catalysts; (e) The density of states (DOS) and (f) partial DOS (PDOS) of the Pd/HSAPO-34 and Pd@CoO/HSAPO-34 catalysts.

O_{lat}/O_{ads} ratio of Pd@CoO/HSAPO-34 (1.09) catalyst is higher than that of other catalysts, which is consistent with the O₂-TPD results (Fig. 2c). Abundant low binding energy oxygen species is confirmed by the higher O_{lat}/O_{ads} ratio, which also suggests the larger electron cloud density over the O atoms [53]. Accordingly, the shift and the difference in the proportion of Pd 3d, Co 2p, and O 1 s peaks further demonstrate the electron transport from Pd NPs to Co species through bridged O (Pd-O-Co coordination) [54]. This electron transfer increases the electron density of oxygen species, and the enhancement of the electron donation promotes oxygen species activation by accepting electrons [55].

Subsequently, the electronic state was evaluated by the projected partial density of states (PDOS) of *d* orbitals in Fig. 3e and 3f. The anchoring of CoO to Pd surface greatly changed the electronic structure of the active sites. Specifically, the observed loss peaks of Pd@CoO/HSAPO-34 catalyst demonstrate a notable contrast when compared to the Pd/HSAPO-34 surface, suggesting the occurrence of electron transfer between the orbitals of Pd, Co, and O species. Moreover, the *d*-band centers of Pd species for Pd/HSAPO-34 and Pd@CoO/HSAPO-34 catalysts are determined as -1.58 and -1.37 eV, respectively, close to the Fermi level ($E_F=0$) to reduce the Pauli repulsion, which results in the

promotion effect of enhanced O₂ adsorption and activation efficiency [56].

3.3. Catalytic performance

The obtained catalysts were further tested for the catalytic oxidation of acetone. As shown in Fig. 4a, the highest efficiency is observed over the Pd@CoO/HSAPO-34 catalyst, where 90 %, 50 %, and 10 % conversion of acetone can be oxidized at 240, 210, and 160 °C, respectively (GHSV of 75,030 mL·g⁻¹·h⁻¹). The temperature of 90 % acetone oxidized (T_{90}) over the prepared catalysts increase with the order of Pd@CoO/HSAPO-34 (240 °C) < Pd/HSAPO-34 (256 °C) < Co/HSAPO-34 (324 °C) < HSAPO-34. According to the above results, it can be found that the efficiency of acetone oxidation is significantly improved by the synthesis of core-shell Pd@CoO Janus active sites. This promotion can be ascribed to the abundant active oxygen species and Pd-O-Co active sites with strengthened electron transformation. The catalytic efficiency of Pd@CoO/HSAPO-34 catalyst is much higher than that of reported representative catalysts, as illustrated in Fig. S8. Furthermore, as shown in Fig. 4b, the 100 % CO₂ selectivity can be achieved at 240 °C over the Pd@CoO/HSAPO-34 catalyst, much higher than that of the Pd/HSAPO-

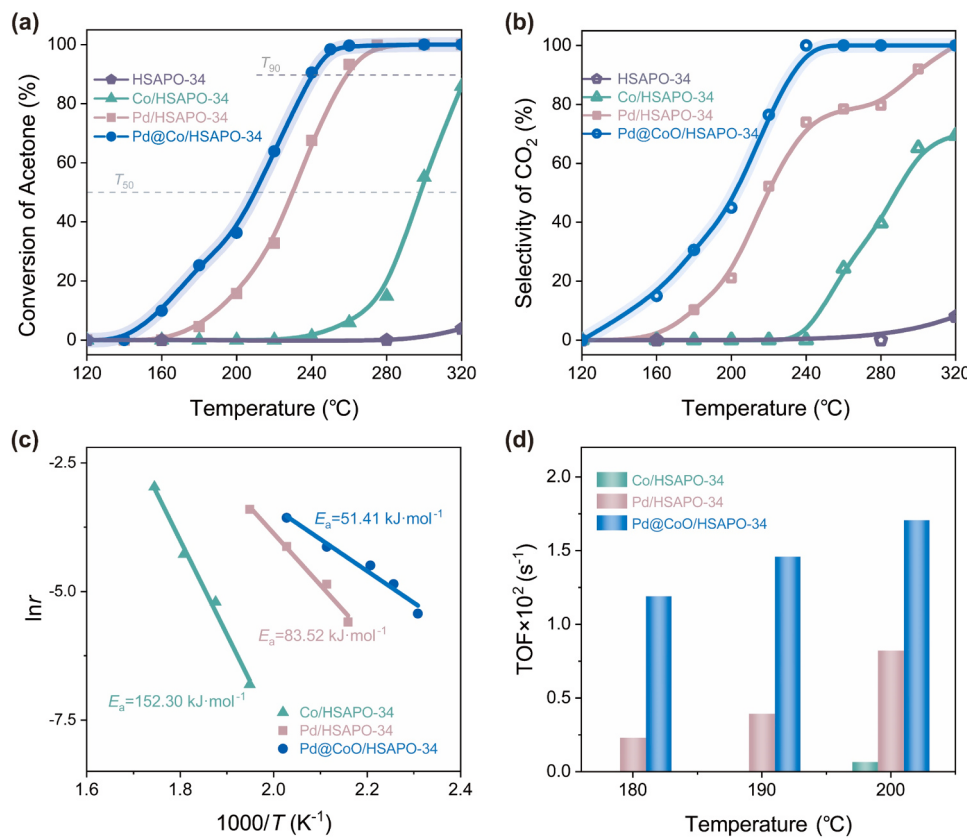


Fig. 4. (a) Activity, (b) CO₂ selectivity, (c) Arrhenius plots, and (d) TOF values for catalytic oxidation of acetone over prepared catalysts.

34 (75 %) and Co/HSAPO-34 (6 %) catalysts at the same temperature.

The apparent activation energy (E_a) was then calculated to evaluate the low-temperature activity of these catalysts, as the catalyst with the lower E_a value would facilitate acetone oxidation more readily. As illustrated in Fig. 4c, the observed strong linearity between the natural logarithm of the rate constant ($\ln k$) and the reciprocal of the reaction temperature provides evidence that the combustion of acetone over the catalysts studied follows a first-order reaction mechanism with regard to acetone concentration, given the specific reaction circumstances used. The E_a values for acetone oxidation over Pd@CoO/HSAPO-34 catalyst ($51.41 \text{ kJ}\cdot\text{mol}^{-1}$) is significantly lower than that of Pd/HSAPO-34 ($83.52 \text{ kJ}\cdot\text{mol}^{-1}$) and Co/HSAPO-34 ($152.30 \text{ kJ}\cdot\text{mol}^{-1}$) catalysts, which can be attributed to significance of core-shell Pd@CoO Janus structure. This trend in reactivity is further evidenced through the consideration of associated turnover frequencies (TOFs) based on the dispersion of Pd sites in Fig. 4d. The TOF of acetone oxidation at 200 °C over Pd@CoO/HSAPO-34 catalyst is determined as 0.017 s^{-1} , 2.6 times higher than that of traditional Pd/HSAPO-34 catalyst.

The stability of catalysts is a crucial factor to be considered when evaluating supported palladium metal catalysts since their susceptibility to high temperature and water-induced deactivations often restricts their long-term utilization in industrial applications. Thus, thermal and hydrothermal stability of these prepared catalysts were further evaluated. The process of thermogravimetric analysis (TG) was used to quantitatively assess the thermal stability and coke formation of these catalysts. The weight-loss zone below 200 °C is attributed to the removal of physically adsorbed H₂O molecules, with an endothermic peak centered at ca. 96 °C for all catalysts [57]. The second weight-loss zone in the range of 200–400 °C, exhibiting a broad endothermic band, can be assigned to the removal of -OH groups in the interior of the lattice and the decomposition of structural water inside the support [58]. The final weight-loss zone in the temperature range between 500 and 600 °C with an exothermic peak at 540 °C is related to the decomposition of coke

deposits, which can only be detected on the Pd/HSAPO-34 catalyst. Generally, the coke is easily formed over the catalysts with abundant strong acid sites during thermal reactions [59]. In this work, there is no significant coke formation, which is related to the decrease of strong acid sites over the fresh and spent Pd@CoO/HSAPO-34 (Fig. S9). Meanwhile, it can be noted that the total weight losses of Pd@CoO/HSAPO-34, Pd/HSAPO-34, and HSAPO-34 catalysts are determined as 19.5 %, 22.8 %, and 23.6 %, respectively. Attributing to the advantages of Pd@CoO Janus core-shell structure, Pd@CoO/HSAPO-34 catalyst displays excellent thermal stability and coking resistance. Moreover, the enhanced adsorption and transformation of surface O₂ species over Pd@CoO/HSAPO-34 catalyst further inhibit the formation of coke during reaction [60]. As depicted in Fig. 5b, the reaction stability of Pd@CoO/HSAPO-34 and Pd/HSAPO-34 catalysts were evaluated in a continuous flow containing 500 ppm acetone at 240 °C for 6 h. It can be observed that the acetone conversion maintained stable during the test, suggesting their outstanding reaction stability.

3.4. Water vapor resistance enhancement

Considering that water vapor always exists in industrial exhaust mixtures, the influence of humidity on the catalytic activity of Pd/HSAPO-34 and Pd@CoO/HSAPO-34 catalysts are displayed in Fig. 5c and 5d. Compared with Pd@CoO/HSAPO-34 catalyst, the acetone conversion for Pd/HSAPO-34 catalyst significantly decreases in the presence of 3 vol% H₂O. The influence of humidity on catalytic activity of Pd/HSAPO-34 and Pd@CoO/HSAPO-34 catalysts when introducing 1 vol% and 3 vol% water vapor into the feed stream at 240 °C (Fig. 5d). Drops in acetone conversion of ca. 12.9 % (from 93 % to 81.5 %) and 32.9 % (from 66.5 % to 44.6 %) are observed over the Pd@CoO/HSAPO-34 and Pd/HSAPO-34 catalysts, respectively, when 3 vol% H₂O is introduced into the stream. When the water vapor is cut off,

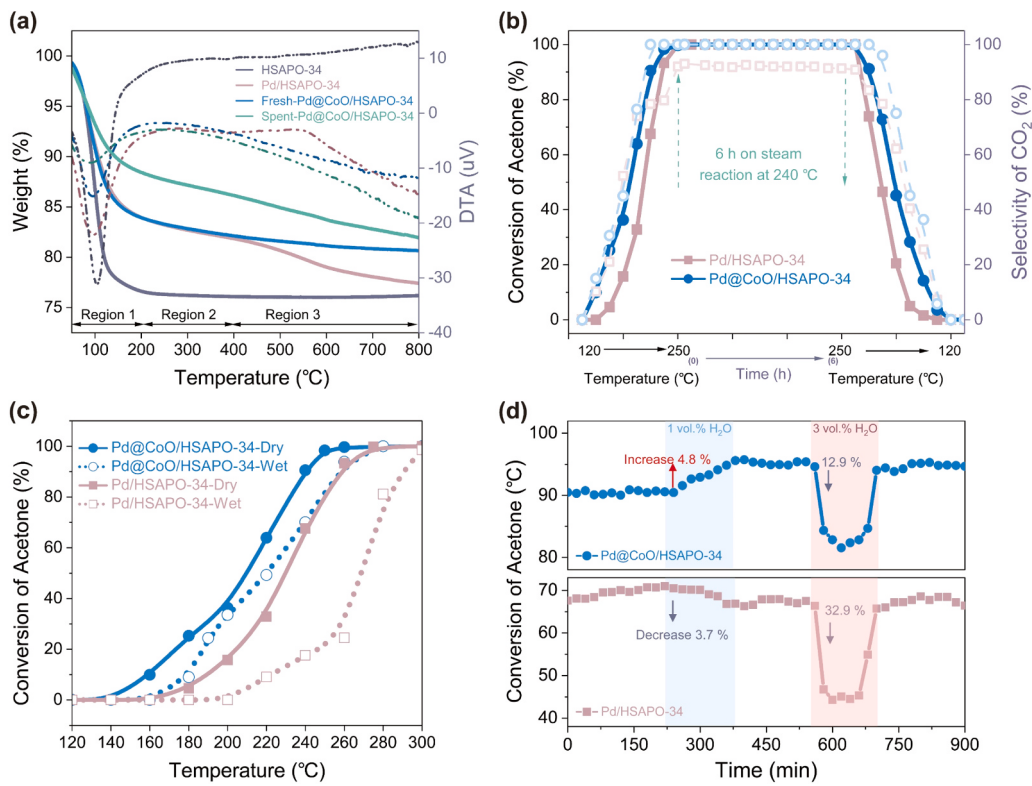


Fig. 5. (a) TG and DTA curves of catalysts; (b) Stability test of catalysts; (c) Light-off curves of prepared catalysts for catalytic oxidation of acetone with and without 3 vol% H₂O; (d) Water-vapor resistance of Pd/HSAPO-34 and Pd@CoO/HSAPO-34 catalysts.

acetone conversion can restore to its original value, suggesting that the catalyst is reversible to the deactivation. For the Pd/HSAPO-34 catalyst, the conversion of acetone in the presence of 1 vol% H₂O decreases from 70.2 % to 66.5 %. Interestingly, the acetone conversion over Pd@CoO/HSAPO-34 increases around 4.8 % (from 90 % to 94.8 %) in the presence of 1 vol% H₂O.

To shed light on the above promotion effect of 1 vol% H₂O over the Pd@CoO/HSAPO-34 catalyst, additional TPD-MS experiments were performed. As shown in Fig. 6a, the peaks located at 175, 169, and 157 °C are ascribed to the desorption of chemically adsorbed acetone species. The large amount of the acetone species desorbed from the Pd@CoO/HSAPO-34 catalyst (as compared with that of Pd/HSAPO-34) suggests that the Pd@CoO Janus sites possess the superb ability for adsorbing acetone molecules. This phenomenon is ascribed to that the presence of positively charged Pd²⁺ species from Pd-CoO interactions can enhance the adsorption and activation of electron-rich C=O bond of the acetone molecules. Subsequently, the H₂O-TPD-MS analysis was implemented to investigate the interaction between H₂O molecules and catalysts surface (Fig. 6b). The desorption peaks of H₂O molecules (*m/z* = 18) were detected in the range of 100–600 °C. The peak below 120 °C is assigned to the H₂O molecules existing in the particle space (“type a” H₂O), which poses weak interaction with the catalyst surface [24,30]. The peak at 190 °C corresponds to the hydroxide through hydrogen bonding or surface-adsorbed H₂O (“type b” H₂O). And the peaks in the range of 250–350 °C are attributed to the associated -HOH (surface hydroxyl groups) species from H₂O molecules over the catalyst surface (“type c” H₂O). The peaks at 506 and 518 °C are assigned to structural hydroxides or H⁺ in tunnel structure (“type d” H₂O). Through peak area fitting evaluation, the presence of “type c” H₂O over Pd@CoO/HSAPO-34 (31.77 %) is higher than that of Pd/HSAPO-34 (27.29 %) catalyst.

The acetone/acetone+H₂O-TPD-MS was further investigated to understand the adsorption and activation properties of acetone and intermediate species on the surface of Pd/HSAPO-34 and Pd@CoO/HSAPO-

34 catalysts. As shown in Fig. 6c, the desorption profiles can be divided into three regions. The peaks at 83 °C correspond to the physically adsorbed acetone species. The peaks centered at 170 and 195 °C can be ascribed to the weakly adsorbed acetone species. The peaks above 300 °C are assigned to the chemically adsorbed acetone species. Obviously, the weak-chemical desorption peak for Pd@CoO/HSAPO-34 catalyst appears at a higher temperature of 192 °C as compared with the Pd/HSAPO-34 catalyst (170 °C). Meanwhile, the peak area of the adsorbed acetone species over Pd@CoO/HSAPO-34 catalyst is slightly larger than that of Pd/HSAPO-34 catalyst (Fig. 6d). The above results illustrate that the Pd@CoO/HSAPO-34 catalyst possesses superb capacity for acetone adsorption [61], in accordance with the acetone-TPD profiles (Fig. 6a). Notably, the desorption peak area of acetone dramatically increases under humid conditions for Pd@CoO/HSAPO-34 (Fig. 6c), indicating that the presence of H₂O species promotes the adsorption of acetone molecules over catalyst surface, attributing to the enhanced dipole-dipole interactions between acetone and surface hydroxyl groups [62]. These results were further proved by the adsorption energy calculated by DFT studies (Fig. 8c).

The CO₂ desorption profiles are shown in Fig. 6e. The desorption peaks below 300 °C are derived from the reaction of acetone with adsorbed oxygen species, and the peaks above 300 °C are derived from the reaction between acetone and lattice oxygen species [63]. The total CO₂ desorption peak area for Pd/HSAPO-34 in the presence of H₂O is lower than that of Pd@CoO/HSAPO-34, indicating that the acetone oxidation is restricted by H₂O over Pd/HSAPO-34 (Fig. 6e and 6f). It can be confirmed that the abundant active oxygen species are regarded as the main reason for the improvement of catalytic activity of Pd@CoO/HSAPO-34 under humid conditions. Furthermore, the enhancement of Pd@CoO/HSAPO-34 performance under humid conditions can be ascribed to the presence of active hydroxyl groups dissociation from H₂O molecules. Above results confirm that the Pd@CoO/HSAPO-34 catalyst with tailored Pd@CoO core-shell Janus sites exhibits the water vapor resistance stability during acetone

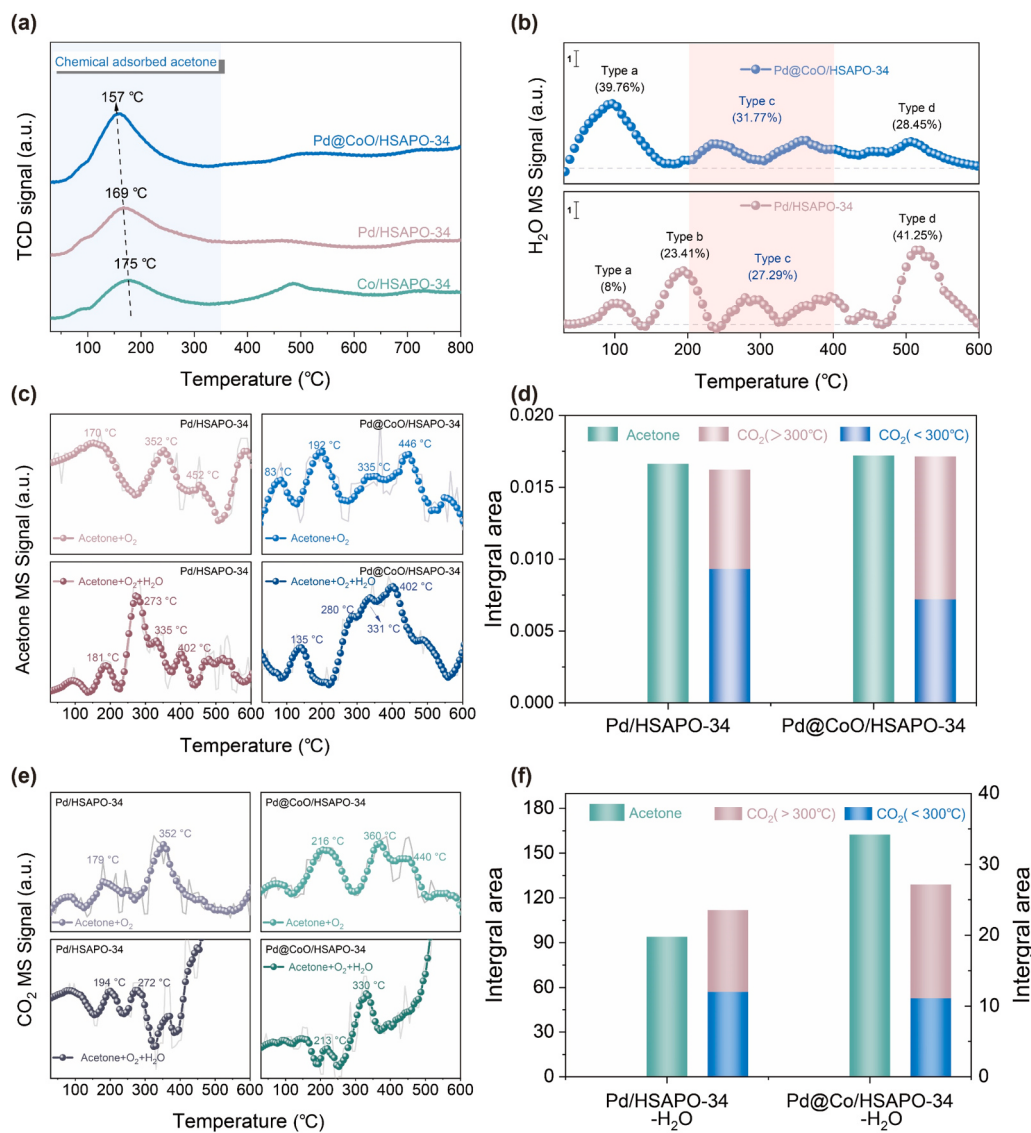


Fig. 6. (a) Acetone-TPD and (b) H₂O-TPD profiles of the synthesized catalysts; (c,e) Acetone and CO₂ desorption profiles from acetone/acetone+H₂O-TPD results, and (d,f) the corresponding integral area analysis of acetone oxidation over prepared catalysts with and without 1 vol% H₂O addition.

oxidation, and demonstrate to be promising in industrial application.

3.5. Synergy of core-shell Pd@CoO Janus sites

To specifically reveal the active sites for acetone activation, the Quasi *in situ* XPS was employed to reveal the specific role of each component during the acetone catalytic reaction. As shown in Fig. 7a and b, the peaks at 335.3–335.7 and 340–340.9 eV are indicative of the Pd⁰ species, and the peaks at 336.5–338 and 342.2–343.3 eV can be assigned to the Pd²⁺ species [45,46]. Notably, for the Pd/HSAPO-34 catalyst (Fig. 7a), the ratio of Pd⁰ species significantly decreases from 52.7 % (fresh sample at room temperature) to 10.7 % (240 °C with 200 ppm acetone) during investigations, attributing to the adsorption and activation of O₂ species over Pd sites. The ratio of Pd⁰ species is slightly replenished (to 22.0 %) after re-exposure to air atmosphere at room temperature. On the contrary, for the Pd@CoO/HSAPO-34 catalyst (Fig. 7b), the ratio of Pd²⁺ species significantly decreases from 51.1 % (fresh sample at room temperature) to 21.3 % (220 °C with 200 ppm acetone) during investigations. The declining proportion of Pd²⁺ species is correlated with the electron transfer from carbonyl groups of acetone molecules to positively charged Pd²⁺ species, which

occurs during the acetone adsorption and activation processes.

The differences in electronegativity of C and O atoms in C=O bond result in an increase of charge density of O atoms over acetone molecules, which assumes an electronegative state. Therefore, the acetone molecules are intended to be activated over the electron-deficient sites. Interestingly, the ratio of Pd²⁺ species is partly replenished (to 41 %) after re-exposure to air atmosphere at room temperature. These observations demonstrate that the positively charged Pd²⁺ species in Pd@CoO Janus sites are superior sites for activating acetone molecules. DFT simulations are performed to further explore the acetone adsorption and activation over the catalysts. The structures of these catalysts with adsorbed acetone are displayed in Fig. 8c, where the acetone adsorption energy (E_{ads}) of Pd@CoO/HSAPO-34 (-1.03 eV) is higher than that of Pd/HSAPO-34 (-0.49 eV).

Subsequently, for the Quasi *in situ* Co 2p XPS spectra (Fig. 7c), the ratio of Co²⁺ species gradually decreases from 62.8 % (fresh sample at room temperature) to 56.4 % (220 °C with 200 ppm acetone) during investigations. Notably, the Co²⁺ species are clearly dominating, which is unsurprising given that this species is known to be pivotal in the oxidation reactions. This result indicates that O₂ species inclines to be adsorbed on the surface of CoO and then activated on surface vacancy,

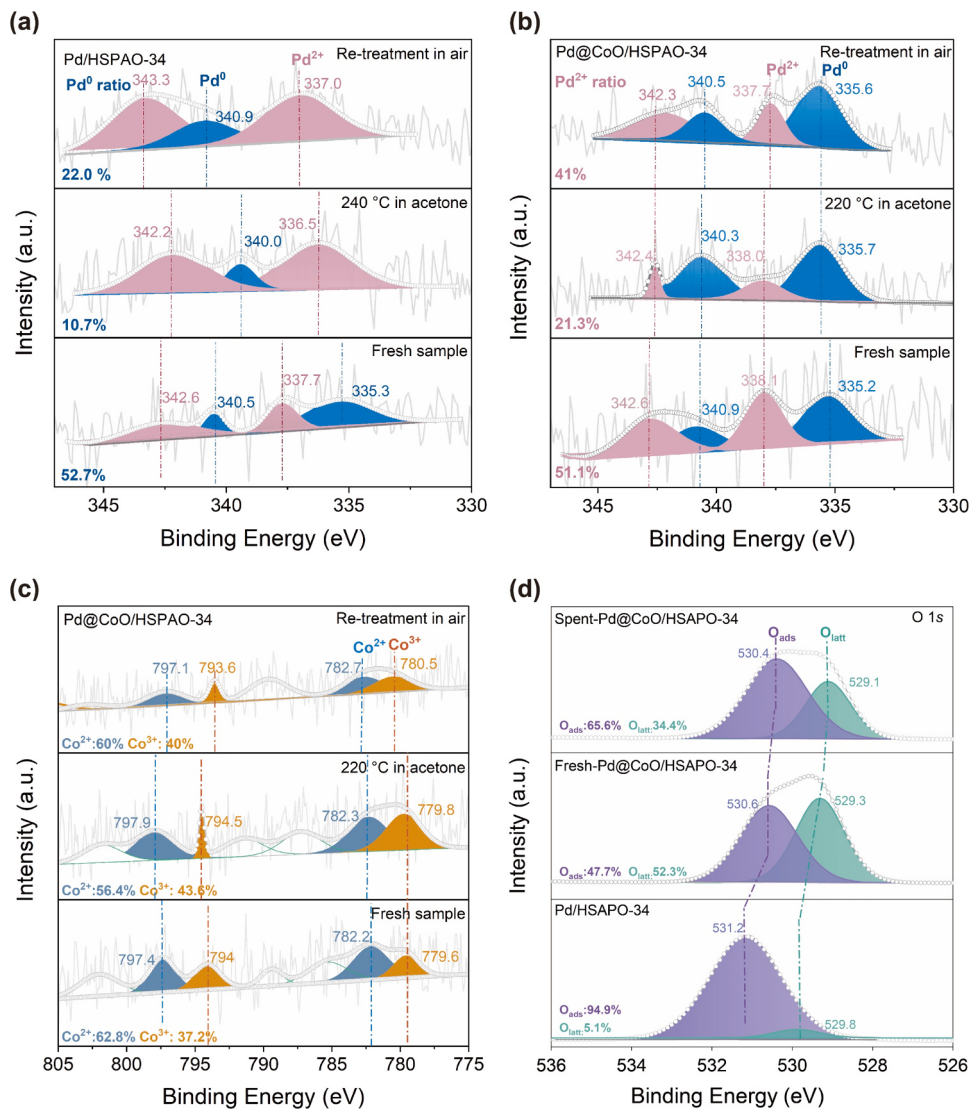


Fig. 7. *In situ* Pd 3d XPS spectra of acetone oxidation over (a) Pd/HSAPO-34 and (b) Pd@CoO/HSAP-34 catalysts; *In situ* Co 2p XPS spectra of acetone oxidation over (c) Pd@CoO/HSAP-34 catalysts; (d) O 1s XPS spectra of representative catalysts.

resulting in an increased valence state of Co atoms over Pd@CoO Janus sites. O 1 s XPS spectra can further evident the activation and transformation of oxygen species, as shown in Fig. 7d. After the reaction, the ratio of O_{latt} species decreases from 52.3 % (fresh Pd@CoO/HSAP-34) to 34.4 % (spent Pd@CoO/HSAP-34). The above *in situ* experiments demonstrate that the Pd²⁺ are preferable sites for activating acetone molecules, and CoO species with weakened Co–O bond are dominating for oxygen species activation. The synergy of core-shell Pd@CoO Janus sites greatly facilitates the low-temperature oxidation of acetone.

3.6. Mechanism investigation

To further investigate the surface reaction intermediates of representative Pd/HSAP-34 and Pd@CoO/HSAP-34 catalysts, *in situ* DRIFTS during acetone oxidation were recorded. The adsorbed acetone (1700–1712 cm⁻¹, the stretching vibration of C=O), formate (1370 cm⁻¹, the vibration of C-H), and deprotonated methanol (1220 cm⁻¹, the stretching vibration of O-H) can be found in Fig. S10. As displayed in the Fig. 8a and 8b, the peak intensity for –COH (1610–1640 cm⁻¹) and C=O (1730 cm⁻¹) species from the surface-adsorbed aldehyde intermediate gradually increases from 120 to 260 °C [64,65]. The hypothesis posits that aldehyde species are formed by

the bonding of uncoordinated carbonyl species with dissociated hydrogen atoms from the CH₃ groups. With an increase in reaction temperature, the asymmetric stretching vibration of (OCO[·]) at 1540–1600 cm⁻¹, the vibration of (C–H) at 1370 cm⁻¹, and the symmetric stretching of v_s(C–H) at 1430–1450 cm⁻¹ appear with the time on steam [66,67]. These bands are attributed to the carboxylate, formate, and acetate species, respectively, indicating the generation of diverse oxygenated intermediates. Importantly, two additional adsorption bands located at 1300 and 1226 cm⁻¹ (ascribed to the absorbed and deprotonated methanol species, respectively) can only be detected over the Pd/HSAP-34 catalyst. These characteristic peaks appear when the temperature reaches 180 °C, and no such band can be observed over the Pd@CoO/HSAP-34 catalyst. This observation indicates that the Pd@CoO Janus site enhances the oxidation of acetone via inhibiting the formation of intermediates (methanol species), resulting in the improvement of its low-temperature efficiency [66,68].

Subsequently, the intermediate products at various temperatures were quantitatively determined by PTR-QMS over Pd@CoO/HSAP-34 and Pd/HSAP-34 catalysts under different reaction conditions, summarized in Fig. 8f and 8j. As detailed in Table S4, the peaks at *m/z* = 45 correspond to the acetaldehyde species. The peaks at *m/z* = 31, 45, and 61 are associated with formaldehyde, acetaldehyde, and acetic acid

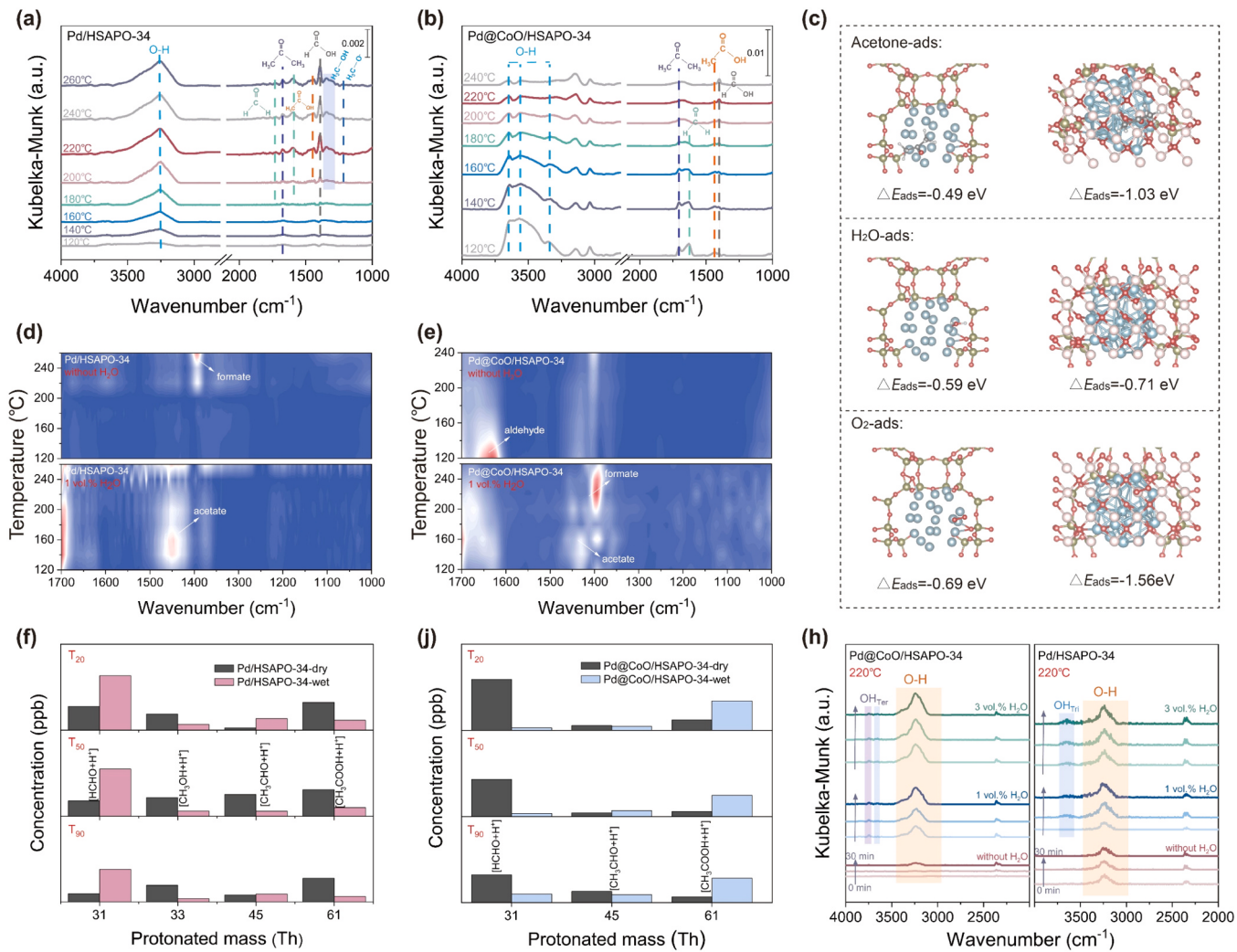


Fig. 8. *In situ* DRIFTS of acetone oxidation over (a) Pd/HSAPO-34 and (b) Pd@CoO/HSAPO-34 catalysts; (c) The optimized structures and calculated energies of acetone, O₂, and H₂O adsorption over Pd/HSAPO-34 (left) and Pd@CoO/HSAPO-34 (right) catalysts; *In situ* DRIFTS of acetone oxidation with 1 vol% H₂O over (d) Pd/HSAPO-34 and (e) Pd@CoO/HSAPO-34 catalysts; (f-j) PTR-QMS results of acetone oxidation with and without 1 vol% H₂O over representative catalysts; (h) *In situ* DRIFTS of acetone oxidation with addition of 1 vol% H₂O over prepared catalysts at 220 °C in the range of 4000–2000 cm⁻¹.

species, respectively. In comparison, for the Pd/HSAPO-34 catalyst, an observed new band can be ascribed to methanol ($m/z = 33$) species, which can only be detected over this catalyst, suggesting an alternative reaction pathway distinct from that of the Pd@CoO/HSAPO-34 catalyst. Furthermore, it is noteworthy that the aldehyde and acetate species are dominating during this reaction, suggesting that the cleavage of these species via deep oxidation processes plays a crucial role during the oxidation of acetone. The obtained results are consistent with the findings of *in situ* DRIFTS (Fig. 8a and 8b).

Additionally, the bands for surface hydroxyl groups are detected in the range of 4000–3000 cm⁻¹. The bands at 3200–3600, 3650, and 3750–3780 cm⁻¹ are attributed to the hydrogen-bonded OH groups, tri-bridged hydroxyl groups (OH_{Tri}), and terminal hydroxyl groups (OH_{Ter}), respectively, demonstrating the activation and dissociation of H₂O molecules [5,69]. Hydrogen dissociated from H₂O molecules will coordinate with oxygen atom of shell-CoO and/or partial core-Pd forming OH_{Tri} and OH_{Ter} groups. For the Pd/HSAPO-34 catalyst (Fig. 8a, 8h, and S11), surface hydroxyl groups intended to competitive adsorption with acetone and continued to accumulate on the surface of catalyst to cover the active sites. As displayed in Fig. 8b, 8h, and S11, the inert hydrogen-bonded hydroxyl group is more easily converted to the active hydroxyl group. In particular, the intensity of peaks representing the surface hydroxyl groups decreases with the increasing temperature

over the Pd@CoO/HSAPO-34 catalyst. Moreover, detailed FT-IR for the fresh and spent catalysts (Fig. S5) reveal that the surface hydroxyl groups of spent Pd@CoO/HSAPO-34 decrease by 25.6 % compared with fresh sample, while the content of spent Pd/HSAPO-34 increases by 30.2 %. It can be seen that H₂O molecule is adsorbed on the surface of the catalyst and then easily dissociated into reactive hydroxyl species due to the abundant oxygen species and the strong Pd-O-Co interaction, which intend to participate in the acetone oxidation reaction, thus improving the water resistance of the Pd@CoO Janus structure catalysts.

In order to further investigate the effect of H₂O on the reaction path of acetone oxidation, the PTR-QMS and *in situ* DRIFTS spectra for catalysts with 1 vol% H₂O introduced were studied. As displayed in Fig. S11, additional by-products are hardly to be detected during the oxidation of acetone in the presence of water vapor, which is consistent with the results obtained in the absence of water vapor. As shown in Fig. 8d and 8f, the peak intensity of acetate species increases over Pd/HSAPO-34 after introducing 1 vol% H₂O, instead formate species is decreased. This result indicates that the introduction of water vapor will inhibit the decomposition of acetate species, thus their accumulation would prevent the formation of formate species, which can be easily oxidized into CO₂ and H₂O [70]. For Pd/HSAPO-34 catalyst, the containing of the H₂O molecules increases the concentration of acetate species, but decreases the concentration of formate species (Fig. 8d).

Interestingly, for Pd@CoO/HSAPO-34 catalyst, the intensity of peak assigned to aldehyde species decreases under the introduction of 1 vol% of water vapor, while the contents of acetate and formate species which are easily mineralized increased (Fig. 8e and 8j).

The electronic structure and adsorption energy were subsequently investigated by DFT calculations. The evaluation includes a range of composite topologies, geometries, and adsorption free energy calculations for acetone, O₂, and H₂O adsorbed on Pd/HSAPO-34 and Pd@CoO/HSAPO-34. As described in Fig. 8c, through a comparative analysis of the initial adsorption energies of acetone and oxygen on two commonly used catalysts, it is evident that both acetone and oxygen exhibit a preference for adsorption onto the surface of the Pd@CoO/HSAPO-34 catalyst. This preference may be attributed to the relatively low adsorption energies observed for acetone (-1.03 eV) and oxygen (-1.56 eV) on this catalyst. The adsorption energy of H₂O molecule exhibits a shift from -0.59 to -0.71 eV, indicating a greater propensity for H₂O adsorption over Pd@CoO/HSAPO-34 catalyst. This enhanced adsorption capability has the potential to facilitate the equilibrium of H₂O activation upon the introduction of water vapor throughout the reaction process.

Accordingly, we propose the possible mechanism during the catalytic oxidation of acetone over the representative catalysts. As given in Fig. 9, the initial step of dehydrogenation accompanies with the formation of CH₂(CH₃)CO* species (* stands for an adsorption atom of the intermediates). Subsequently, the vicinal C-C bonds are cleaved, which is promoted by the electron deficient carbonyl groups, leading to the formation of CH₃CHO* species. Differently, the CH₃CHO* would transform into CH₃OH* via α -H abstraction process, which only appears over the Pd/HSAPO-34 catalyst. The CH₃CHO* and CH₃OH* species are further dissociated and/or desorbed to generate CH₂O* and/or CH₃CHO (gas). Finally, the CH₂O* group was attacked by dissociated and activated oxygen (O*) to form COO⁻ adsorbed species and further dehydrogenation occurred through α -H abstraction and C-C cleavage, yielding harmless H₂O and CO₂. Specifically, when 1 vol% H₂O was introduced, for the Pd/HSAPO-34 catalyst, the H₂O molecules on the surface of the catalyst will easily cover the initial active sites and pose competitive adsorption, resulting in the formation of more intermediates and inhibition of reaction path. While, for the Pd@CoO/HSAPO-34 catalyst, the adsorbed aldehyde species are attacked by the reactive hydroxyl groups dissociated from H₂O molecules to form acetate and formate species (CH₃-OCO- and H-OCO-). Therefore, the synthesized Pd@CoO Janus boosts the oxidizing efficiency and H₂O dissociation, which are beneficial for the complete oxidation of acetone.

4. Conclusions

In summary, the Pd@CoO/HSAPO-34 catalyst containing core-shell Janus sites with tailored local coordination structures was designed and synthesized through a two-step thermal-depolymerization method. This prepared Pd@CoO/HSAPO-34 catalyst exhibits outstanding efficiency for the catalytic oxidation of acetone, over which 500 ppm of acetone can be fully oxidized at 240 °C with a GHSV of 75,030 mL·g⁻¹·h⁻¹. The determined structure-activity relationships reveal that the interactions between Pd sites and CoO shell promote charge redistribution and electron back-donation through Pd-O-Co coordination. Therefore, abundant positively charged Pd²⁺ active sites are formed and the oxygen species transformation is facilitated. Importantly, the core-shell Pd@CoO Janus sites can greatly facilitate the dissociation of H₂O molecules to active surface -OH groups. The generated reactive OH_{Ter} and OH_{Tri} species (hydrogenated O_{latt}) can significantly promote the rapid conversion of aldehyde by-products via attacking the CH₂O* group, which in-turn promotes the acetone being fully oxidized at low-temperatures. This work helps to establish a foundational comprehension of the key significance for improving the catalytic performance of supported catalysts under industrial humid conditions.

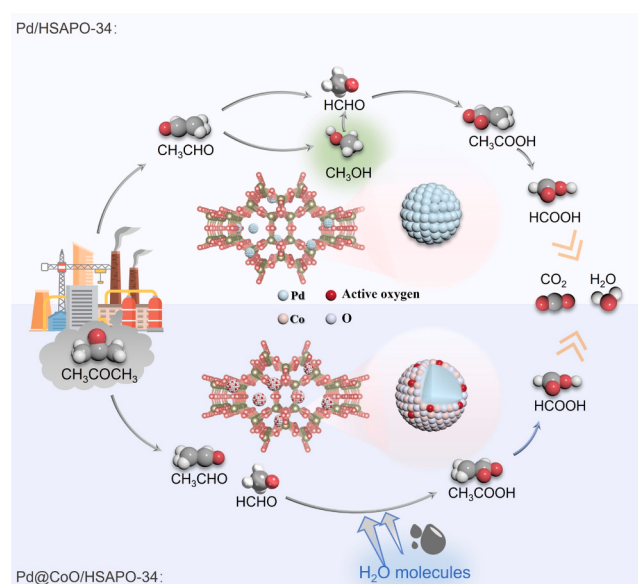


Fig. 9. Schematic illustration of the reaction pathways for catalytic oxidation of acetone over Pd@CoO/HSAPO-34 and Pd/HSAPO-34 catalysts.

CRediT authorship contribution statement

Wu Yani: Conceptualization, Data curation, Investigation, Visualization, Writing-original draft. **Wang Yadi:** Formal analysis, Visualization, Investigation. **Liu Jicheng:** Investigation, Formal analysis, Visualization. **Jiang Zeyu:** Conceptualization, Formal analysis, Data curation, Resources, Validation, Writing-original draft. **Wan Jialei:** Formal analysis, Investigation. **Wang Jingjing:** Conceptualization, Formal analysis. **Chai Shouning:** Software, Writing-review & editing. **Ai Chunli:** Formal analysis, Investigation. **Dang Fan:** Validation, Visualization. **Reem Albilal:** Writing-review & editing. **He Chi:** Conceptualization, Funding acquisition, Supervision, Writing-review & editing.

Declaration of Competing Interest

The authors declare that they have no known competing financial interests or personal relationships that could have appeared to influence the work reported in this paper.

Data availability

Data will be made available on request.

Acknowledgements

This work was financially supported by the National Natural Science Foundation of China (22276145, 21922606), the National Key R&D Program of China (2022YFB4101500). The authors gratefully acknowledge the support of K.C. Wong Education Foundation and instrumental analysis center of Xi'an Jiaotong University.

Appendix A. Supporting information

Supplementary data associated with this article can be found in the online version at doi:10.1016/j.apcatb.2024.124113.

References

- [1] C. He, J. Cheng, X. Zhang, M. Douthwaite, S. Pattisson, Z. Hao, Recent advances in the catalytic oxidation of volatile organic compounds: a review based on pollutant sorts and sources, Chem. Rev. 119 (2019) 4471–4568, <https://doi.org/10.1021/acs.chemrev.8b00408>.

- [2] Z. Jiang, Y. Wang, C. Chen, C. He, Progress and challenge of functional single-atom catalysts for the catalytic oxidation of volatile organic compounds, *Chin. Chem. Lett.* (2023) 109400, <https://doi.org/10.1016/j.cclet.2023.109400>.
- [3] A. Mellouki, T.J. Wallington, J. Chen, Atmospheric chemistry of oxygenated volatile organic compounds: impacts on air quality and climate, *Chem. Rev.* 115 (2015) 3984–4014, <https://doi.org/10.1021/cr500549n>.
- [4] C. Yang, G. Miao, Y. Pi, Q. Xia, J. Wu, Z. Li, J. Xiao, Abatement of various types of VOCs by adsorption/catalytic oxidation: a review, *Chem. Eng. J.* 370 (2019) 1128–1153, <https://doi.org/10.1016/j.cej.2019.03.232>.
- [5] J. Guo, C. Lin, C. Jiang, P. Zhang, Review on noble metal-based catalysts for formaldehyde oxidation at room temperature, *Appl. Surf. Sci.* 475 (2019) 237–255, <https://doi.org/10.1016/j.japsusc.2018.12.238>.
- [6] T. Dong, W. Liu, M. Ma, H. Peng, S. Yang, J. Tao, C. He, L. Wang, P. Wu, T. An, Hierarchical zeolite enveloping Pd-CeO₂ nanowires: an efficient adsorption/catalysis bifunctional catalyst for low temperature propane total degradation, *Chem. Eng. J.* 393 (2020) 124717, <https://doi.org/10.1016/j.cej.2020.124717>.
- [7] M. Ma, Y. Jian, C. Chen, C. He, Spherical-like Pd/SiO₂ catalysts for n-butylamine efficient combustion: effect of support property and preparation method, *Catal. Today* 339 (2020) 181–191, <https://doi.org/10.1016/j.cattod.2018.11.024>.
- [8] Y. Long, Q. Meng, M. Chen, X. Luo, Q. Dai, H. Lu, Z. Wu, X. Weng, Selective Ru adsorption on SnO₂/CeO₂ mixed oxides for efficient destruction of multicomponent volatile organic compounds: from laboratory to practical possibility, *Environ. Sci. Technol.* 56 (2022) 9762–9772, <https://doi.org/10.1021/acs.est.2c02925>.
- [9] K. Zhang, L. Dai, Y. Liu, J. Deng, L. Jing, K. Zhang, Z. Hou, X. Zhang, J. Wang, Y. Feng, Y. Zhang, H. Dai, Insights into the active sites of chlorine-resistant Pt-based bimetallic catalysts for benzene oxidation, *Appl. Catal. B: Environ.* 279 (2020) 119372, <https://doi.org/10.1016/j.apcatb.2020.119372>.
- [10] X. Zhang, L. Dai, Y. Liu, J. Deng, L. Jing, Z. Wang, W. Pei, X. Yu, J. Wang, H. Dai, Effect of support nature on catalytic activity of the bimetallic RuCo nanoparticles for the oxidative removal of 1,2-dichloroethane, *Appl. Catal. B: Environ.* 285 (2021) 119804, <https://doi.org/10.1016/j.apcatb.2020.119804>.
- [11] M. Ma, R. Yang, C. He, Z. Jiang, J.-W. Shi, R. Albilali, K. Fayaz, B. Liu, Pd-based catalysts promoted by hierarchical porous Al₂O₃ and ZnO microsphere supports/coatings for ethyl acetate highly active and stable destruction, *J. Hazard. Mater.* 401 (2021) 123281, <https://doi.org/10.1016/j.jhazmat.2020.123281>.
- [12] M. He, Y. Cao, J. Ji, K. Li, H. Huang, Superior catalytic performance of Pd-loaded oxygen-vacancy-rich TiO₂ for formaldehyde oxidation at room temperature, *J. Catal.* 396 (2021) 122–135, <https://doi.org/10.1016/j.jcat.2021.01.035>.
- [13] C. Zhang, Y. Li, Y. Wang, H. He, Sodium-promoted Pd/TiO₂ for catalytic oxidation of formaldehyde at ambient temperature, *Environ. Sci. Technol.* 48 (2014) 5816–5822, <https://doi.org/10.1021/es4056627>.
- [14] Q. Zhao, Y. Ge, K. Fu, Y. Zheng, Q. Liu, C. Song, N. Ji, D. Ma, Catalytic performance of the Pd/TiO₂ modified with MnO_x catalyst for acetone total oxidation, *Appl. Surf. Sci.* 496 (2019) 143579, <https://doi.org/10.1016/j.apsusc.2019.143579>.
- [15] L. Yue, C. He, X. Zhang, P. Li, Z. Wang, H. Wang, Z. Hao, Catalytic behavior and reaction routes of MEK oxidation over Pd/ZSM-5 and Pd-Ce/ZSM-5 catalysts, *J. Hazard. Mater.* 244–245 (2013) 613–620, <https://doi.org/10.1016/j.jhazmat.2012.10.048>.
- [16] M. Kraus, U. Trommler, F. Holzer, F.-D. Kopinke, U. Roland, Competing adsorption of toluene and water on various zeolites, *Chem. Eng. J.* 351 (2018) 356–363, <https://doi.org/10.1016/j.cej.2018.06.128>.
- [17] Z. Jiang, C. He, N.F. Dummer, J. Shi, M. Tian, C. Ma, Z. Hao, S.H. Taylor, M. Ma, Z. Shen, Insight into the efficient oxidation of methyl-ethyl-ketone over hierarchically micro-messtructured Pt/K-Al₂O₃ nanorod catalysts: structure-activity relationships and mechanism, *Appl. Catal. B: Environ.* 226 (2018) 220–233, <https://doi.org/10.1016/j.apcatb.2017.12.007>.
- [18] C. He, Z. Jiang, M. Ma, X. Zhang, M. Douthwaite, J.-W. Shi, Z. Hao, Understanding the promotional Effect of Mn₂O₃ on micro-/mesoporous hybrid silica nanocubic-supported Pt catalysts for the low-temperature destruction of Methyl Ethyl Ketone: an experimental and theoretical study, *ACS Catal.* 8 (2018) 4213–4229, <https://doi.org/10.1021/acscat.7b04461>.
- [19] J. Wang, P. Zhang, J. Li, C. Jiang, R. Yunus, J. Kim, Room-temperature oxidation of formaldehyde by layered manganese oxide: effect of water, *Environ. Sci. Technol.* 49 (2015) 12372–12379, <https://doi.org/10.1021/acs.est.5b02085>.
- [20] M. Xiao, D. Han, X. Yang, N. Tsoma Tchinda, L. Du, Y. Guo, Y. Wei, X. Yu, M. Ge, Ni-doping-induced oxygen vacancy in Pt-CeO₂ catalyst for toluene oxidation: enhanced catalytic activity, water-resistance, and SO₂-tolerance, *Appl. Catal. B: Environ.* 323 (2023) 122173, <https://doi.org/10.1016/j.apcatb.2022.122173>.
- [21] M. Ma, R. Yang, Z. Jiang, C. Chen, Q. Liu, R. Albilali, C. He, Fabricating M/Al₂O₃/cordierite (M = Cr, Mn, Fe, Co, Ni and Cu) monolithic catalysts for ethyl acetate efficient oxidation: unveiling the role of water vapor and reaction mechanism, *Fuel* 303 (2021) 121244, <https://doi.org/10.1016/j.fuel.2021.121244>.
- [22] J. Deng, W. Song, L. Chen, L. Wang, M. Jing, Y. Ren, Z. Zhao, J. Liu, The effect of oxygen vacancies and water on HCHO catalytic oxidation over Co₃O₄ catalyst: a combination of density functional theory and microkinetic study, *Chem. Eng. J.* 355 (2019) 540–550, <https://doi.org/10.1016/j.cej.2018.08.195>.
- [23] X. Zhang, F. Bi, Z. Zhu, Y. Yang, S. Zhao, J. Chen, X. Lv, Y. Wang, J. Xu, N. Liu, The promoting effect of H₂O on rod-like MnCeO_x derived from MOFs for toluene oxidation: a combined experimental and theoretical investigation, *Appl. Catal. B: Environ.* 297 (2021) 120393, <https://doi.org/10.1016/j.apcatb.2021.120393>.
- [24] C. Ma, C. Yang, B. Wang, C. Chen, F. Wang, X. Yao, M. Song, Effects of H₂O on HCHO and CO oxidation at room-temperature catalyzed by MC₂O₄ (M=Mn, Ce and Cu) materials, *Appl. Catal. B: Environ.* 254 (2019) 76–85, <https://doi.org/10.1016/j.apcatb.2019.04.085>.
- [25] D. Ma, W. Liu, Y. Huang, D. Xia, Q. Lian, C. He, Enhanced catalytic ozonation for eliminating CH₃SH via stable and circular electronic metal-support interactions of Si-O-Mn bonds with low Mn loading, *Environ. Sci. Technol.* 56 (2022) 3678–3688, <https://doi.org/10.1021/acs.est.1c07065>.
- [26] B. Zhang, L. Zhou, M. Qi, Z. Li, J. Han, K. Li, Y. Zhang, F. Dehgani, R. Liu, J. Yun, Outstanding stability and enhanced catalytic activity for toluene oxidation by Si-O-Mn interaction over MnO_x/SiO₂, *Ind. Eng. Chem. Res.* 61 (2022) 1044–1055, <https://doi.org/10.1021/acs.iecr.1c02504>.
- [27] L. Li, N. Zhang, R. Wu, L. Song, G. Zhang, H. He, Comparative study of moisture-treated Pd@CeO₂/Al₂O₃ and Pd/CeO₂/Al₂O₃ catalysts for automobile exhaust emission reactions: effect of core-shell interface, *ACS Appl. Mater. Interfaces* 12 (2020) 10350–10358, <https://doi.org/10.1021/acsami.9b20734>.
- [28] D. Gu, C.-J. Jia, C. Weidenthaler, H.-J. Bongard, B. Spliethoff, W. Schmidt, F. Schüth, Highly ordered mesoporous cobalt-containing oxides: structure, catalytic properties, and active sites in oxidation of carbon monoxide, *J. Am. Chem. Soc.* 137 (2015) 11407–11418, <https://doi.org/10.1021/jacs.5b06336>.
- [29] K. Qian, Y. Yan, S. Xi, T. Wei, Y. Dai, X. Yan, H. Kobayashi, S. Wang, W. Liu, R. Li, Elucidating the strain-vacancy-activity relationship on structurally deformed Co@CoO nanosheets for aqueous phase reforming of formaldehyde, *Small* 17 (2021) 2102970, <https://doi.org/10.1002/smll.202102970>.
- [30] M. Jiang, D. Yan, X. Lv, Y. Gao, H. Jia, Recognition of water-dissociation effect toward lattice oxygen activation on single-atom Co catalyst in toluene oxidation, *Appl. Catal. B: Environ.* 319 (2022) 121962, <https://doi.org/10.1016/j.apcatb.2022.121962>.
- [31] J. Shan, Y. Xue, D. Wang, Z. Chen, S. Zhu, Direct production of ethanol with high yield from glycerol via synergistic catalysis by Pd/CoO_x and Cu/SBA-15, *Appl. Catal. B: Environ.* 302 (2022) 120870, <https://doi.org/10.1016/j.apcatb.2021.120870>.
- [32] J. Luo, Y. Liu, L. Zhang, Y. Ren, S. Miao, B. Zhang, D.S. Su, C. Liang, Atomic-scale observation of bimetallic Au-CuO_x nanoparticles and their interfaces for activation of CO molecules, *ACS Appl. Mater. Interfaces* 11 (2019) 35468–35478, <https://doi.org/10.1021/acsami.9b12017>.
- [33] M. Chaghband, M. Haghghi, S. Saedy, S. Aghamohammadi, Efficient hydrothermal synthesis of nanostructured SAPO-34 using ultrasound energy: Physicochemical characterization and catalytic performance toward methanol conversion to light olefins, *Adv. Powder Technol.* 25 (2014) 1728–1736, <https://doi.org/10.1016/j.ap.2014.06.022>.
- [34] Q. Wang, M. Shen, J. Wang, C. Wang, J. Wang, Nature of cerium on improving low-temperature hydrothermal stability of SAPO-34, *J. Rare Earths* 39 (2021) 548–557, <https://doi.org/10.1016/j.jre.2020.06.018>.
- [35] M. Ma, H. Huang, C. Chen, Q. Zhu, L. Yue, R. Albilali, C. He, Highly active SBA-15-confined Pd catalyst with short rod-like micro-mesoporous hybrid nanostructure for n-butylamine low-temperature destruction, *Mol. Catal.* 455 (2018) 192–203, <https://doi.org/10.1016/j.mcat.2018.06.016>.
- [36] L. Tao, G. Zhao, P. Chen, Z. Zhang, Y. Liu, Y. Lu, Thin-felt microfibrous-structured Au- α -Fe₂O₃/ns- γ -Al₂O₃/Al-fiber catalyst for high-throughput CO oxidation, *Appl. Catal. A: Gen.* 556 (2018) 180–190, <https://doi.org/10.1016/j.apcata.2018.03.003>.
- [37] X. Mu, H. Ding, W. Pan, P. Zhou, W. Du, K. Qiu, J. Ma, K. Zhang, Research progress in catalytic oxidation of volatile organic compound acetone, *J. Environ. Chem. Eng.* 9 (2021) 105650, <https://doi.org/10.1016/j.je.2021.105650>.
- [38] J. Yang, S. Hu, Y. Fang, S. Hoang, L. Li, W. Yang, Z. Liang, J. Wu, J. Hu, W. Xiao, C. Pan, Z. Luo, J. Ding, L. Zhang, Y. Guo, Oxygen vacancy promoted O₂ activation over perovskite oxide for low-temperature CO oxidation, *ACS Catal.* 9 (2019) 9751–9763, <https://doi.org/10.1021/acs.cat.9b02408>.
- [39] C. Shan, Y. Zhang, Q. Zhao, K. Fu, Y. Zheng, R. Han, C. Liu, N. Ji, W. Wang, Q. Liu, Acid etching-induced in situ growth of λ -MnO₂ over CoMn spinel for low-temperature volatile organic compound oxidation, *Environ. Sci. Technol.* 56 (2022) 10381–10390, <https://doi.org/10.1021/acs.est.2c02483>.
- [40] X. Duan, T. Zhao, B. Niu, Z. Wei, G. Li, Z. Zhang, J. Cheng, Z. Hao, Simultaneously constructing active sites and regulating Mn-O strength of Ru-supported perovskite for efficient oxidation and hydrolysis oxidation of chlorobenzene, *Adv. Sci.* 10 (2023) 2205054, <https://doi.org/10.1002/advs.202205054>.
- [41] L. Xia, S. Xu, Y. Jian, X. Feng, Z. Jiang, J. Wang, Y. Li, Y. Wang, S. Chai, Y. Liu, H. Peng, R. Albilali, C. He, Efficient propane mineralization over unsaturated Pd cluster/CeO₂ with prominent C-C cleavage capacity driven by inherent oxygen activation ability, *J. Hazard. Mater.* 461 (2024) 132509. (<https://www.sciencedirect.com/science/article/pii/S0304389423017922>)
- [42] Q. Huang, P. Zhao, L. Lv, W. Zhang, B. Pan, Redox-induced in situ growth of MnO₂ with rich oxygen vacancies over monolithic copper foam for boosting toluene combustion, *Environ. Sci. Technol.* 57 (2023) 9096–9104, <https://doi.org/10.1021/acs.est.3c02103>.
- [43] G. Shen, R. Zhang, L. Pan, F. Hou, Y. Zhao, Z. Shen, W. Mi, C. Shi, Q. Wang, X. Zhang, J. Zou, Regulating the spin state of Fe^{III} by atomically anchoring on ultrathin titanium dioxide for efficient oxygen evolution electrocatalysis, *Angew. Chem. Int. Ed.* 132 (2019) 2333–2337, <https://doi.org/10.1002/ange.201913080>.
- [44] X. Duan, T. Zhao, Z. Yang, B. Niu, G. Li, B. Li, Z. Zhang, J. Cheng, Z. Hao, Oxygen activation-boosted manganese oxide with unique interface for chlorobenzene oxidation: unveiling the roles and dynamic variation of active oxygen species in heterogeneous catalytic oxidation process, *Appl. Catal. B: Environ.* 331 (2023) 122719, <https://doi.org/10.1016/j.apcatb.2023.122719>.
- [45] A. Wang, X. He, X. Lu, H. Xu, Y. Tong, G. Li, Palladium–cobalt nanotube arrays supported on carbon fiber cloth as high-performance flexible electrocatalysts for ethanol oxidation, *Angew. Chem. Int. Ed.* 127 (2015) 3740–3744, <https://doi.org/10.1002/ange.201410792>.
- [46] X. Lu, C. Guo, M. Zhang, L. Leng, J.H. Horton, W. Wu, Z. Li, Rational design of palladium single-atoms and clusters supported on silicoaluminophosphate-31 by a

- photochemical route for chemoselective hydrodeoxygenation of vanillin, *Nano Res.* 14 (2021) 4347–4355, <https://doi.org/10.1007/s12274-021-3857-2>.
- [47] Y. Jian, M. Tian, C. He, J. Xiong, Z. Jiang, H. Jin, L. Zheng, R. Albilali, J.-W. Shi, Efficient propane low-temperature destruction by Co_3O_4 crystal facets engineering: Unveiling the decisive role of lattice and oxygen defects and surface acid-base pairs, *Appl. Catal. B: Environ.* 283 (2021) 119657, <https://doi.org/10.1016/j.apcatb.2020.119657>.
- [48] Z. Jiang, X. Feng, J. Deng, C. He, M. Douthwaite, Y. Yu, J. Liu, Z. Hao, Z. Zhao, Atomic-scale insights into the low-temperature oxidation of methanol over a single-atom $\text{Pt}_{1-\text{x}}\text{Co}_3\text{O}_4$ catalyst, *Adv. Funct. Mater.* 29 (2019) 1902041, <https://doi.org/10.1002/adfm.201902041>.
- [49] X. Han, G. He, Y. He, J. Zhang, X. Zheng, L. Li, C. Zhong, W. Hu, Y. Deng, T.-Y. Ma, Engineering catalytic active sites on cobalt oxide surface for enhanced oxygen electrocatalysis, *Adv. Energy Mater.* 8 (2018) 1702222. (<https://onlinelibrary.wiley.com/doi/abs/10.1002/aenm.201702222>).
- [50] Q. Zhao, Q. Liu, C. Song, N. Ji, D. Ma, X. Lu, Enhanced catalytic performance for VOCs oxidation on the CoAlO oxides by KMnO_4 doped on facile synthesis, *Chemosphere* 218 (2019) 895–906, <https://doi.org/10.1016/j.chemosphere.2018.11.131>.
- [51] H. Tan, J. Wang, S. Yu, K. Zhou, Support morphology-dependent catalytic activity of Pd/CeO_2 for formaldehyde oxidation, *Environ. Sci. Technol.* 49 (2015) 8675–8682, <https://doi.org/10.1021/acs.est.5b01264>.
- [52] Y. Wang, A.-P. Jia, M.-F. Luo, J.-Q. Lu, Highly active spinel type CoCr_2O_4 catalysts for dichloromethane oxidation, *Appl. Catal. B: Environ.* 165 (2015) 477–486, <https://doi.org/10.1016/j.apcatb.2014.10.044>.
- [53] Y. Li, Y. Men, S. Liu, J. Wang, K. Wang, Y. Tang, W. An, X. Pan, L. Li, Remarkably efficient and stable $\text{Ni}/\text{Y}_2\text{O}_3$ catalysts for CO_2 methanation: Effect of citric acid addition, *Appl. Catal. B: Environ.* 293 (2021) 120206. (<https://www.sciencedirect.com/science/article/pii/S0926337321003325>).
- [54] W.-P. Zhang, J.-R. Li, Y.-Y. Li, J. Zhao, K. Wu, H. Xiao, C. He, Acetone efficient degradation under simulated humid conditions by Mn-O-Pt interaction taming-triggered water dissociation intensification, *Environ. Sci. Technol.* 57 (2023) 20962–20973, <https://doi.org/10.1021/acs.est.3c07194>.
- [55] R.A.L. Baylon, J. Sun, L. Kovarik, M. Engelhard, H. Li, A.D. Winkelman, Y. Wang, Structural identification of ZnxZrOyZ catalysts for Cascade aldolization and self-deoxygenation reactions, *Appl. Catal. B: Environ.* 234 (2018) 337–346, <https://doi.org/10.1016/j.apcatb.2018.04.051>.
- [56] X. Cheng, Y. Wang, Y. Lu, L. Zheng, S. Sun, H. Li, G. Chen, J. Zhang, Single-atom alloy with Pt-Co dual sites as an efficient electrocatalyst for oxygen reduction reaction, *Appl. Catal. B: Environ.* 306 (2022) 121112, <https://doi.org/10.1016/j.apcatb.2022.121112>.
- [57] M. Tian, X. Guo, R. Dong, Z. Guo, J. Shi, Y. Yu, M. Cheng, R. Albilali, C. He, Insight into the boosted catalytic performance and chlorine resistance of nanosphere-like meso-macroporous $\text{CrO}_x/\text{MnCo}_3\text{O}_x$ for 1,2-dichloroethane destruction, *Appl. Catal. B: Environ.* 259 (2019) 118018, <https://doi.org/10.1016/j.apcatb.2019.118018>.
- [58] C. Chen, Y. Yu, C. He, L. Wang, H. Huang, R. Albilali, J. Cheng, Z. Hao, Efficient capture of CO_2 over ordered micro-mesoporous hybrid carbon nanosphere, *Appl. Surf. Sci.* 439 (2018) 113–121, <https://doi.org/10.1016/j.apsusc.2017.12.217>.
- [59] Z. Jiang, R. Dong, M. Tian, C. He, Y. Wu, M. Ma, S. Chai, Achieving acetone efficient deep decomposition by strengthening reactants adsorption and activation over difunctional $\text{Au}(\text{OH})\text{K}_x/\text{hierarchical MFI}$ catalyst, *J. Colloid Interface Sci.* 612 (2022) 504–515, <https://doi.org/10.1016/j.jcis.2021.12.184>.
- [60] S. Das, A. Jangam, S. Xi, A. Borgna, K. Hidajat, S. Kawi, Highly Dispersed Ni/Silica by carbonization–calcination of a chelated precursor for coke-free dry reforming of methane, *ACS Appl. Energy Mater.* 3 (2020) 7719–7735, <https://doi.org/10.1021/acsaem.0c01122>.
- [61] B. Li, H. Xiong, W. Dai, Z. Huang, X. Zhong, J. Zhang, L. Zhou, K. Wu, J. Zou, X. Luo, Enabling the activation of lattice oxygen and high distribution of Co^{3+} on LaCo_3 surface through fluorine incorporation to promote toluene combustion, *Appl. Catal. B: Environ.* 347 (2024) 123828, <https://doi.org/10.1016/j.apcatb.2024.123828>.
- [62] J.-R. Li, W.-P. Zhang, J. Zhao, M. Tian, K. Wu, H. Xiao, C. He, Accelerating the low-temperature catalytic oxidation of acetone over Al-substituted Mn-Al oxides by rate-limiting step modulation, *ACS Appl. Mater. Interfaces* 14 (2022) 36536–36550, <https://doi.org/10.1021/acsmi.2c06186>.
- [63] H. Chen, Y. Liu, R. Gao, T. Dong, Z. Hou, L. Jing, E. Duan, J. Deng, H. Dai, N-doped carbon-modified palladium catalysts with superior water-resistant performance for the oxidative removal of toxic aromatics, *J. Hazard. Mater.* 437 (2022) 129358, <https://doi.org/10.1016/j.jhazmat.2022.129358>.
- [64] Z. Yan, Z. Xu, B. Cheng, C. Jiang, Co_3O_4 nanorod-supported Pt with enhanced performance for catalytic HCHO oxidation at room temperature, *Appl. Surf. Sci.* 404 (2017) 426–434, <https://doi.org/10.1016/j.apsusc.2017.02.010>.
- [65] H. Alalwan, A. Alminshid, An in-situ DRIFTS study of acetone adsorption mechanism on TiO_2 nanoparticles, *Acta Mol. Biomol. Spectrosc.* 229 (2020) 117990, <https://doi.org/10.1016/j.saa.2019.117990>.
- [66] Z. Hu, Z. Wang, Y. Guo, L. Wang, Y. Guo, J. Zhang, W. Zhan, Total oxidation of propane over a Ru/ CeO_2 catalyst at low temperature, *Environ. Sci. Technol.* 52 (2018) 9531–9541, <https://doi.org/10.1021/acs.est.8b03448>.
- [67] D.W. Kwon, P.W. Seo, G.J. Kim, S.C. Hong, Characteristics of the HCHO oxidation reaction over Pt/ TiO_2 catalysts at room temperature: The effect of relative humidity on catalytic activity, *Appl. Catal. B: Environ.* 163 (2015) 436–443, <https://doi.org/10.1016/j.apcatb.2014.08.024>.
- [68] V. Muravev, J.F.M. Simons, A. Parastaei, M.A. Verheijen, J.J.C. Struijs, N. Kosinov, E.J.M. Hensen, Operando spectroscopy unveils the catalytic role of different palladium oxidation states in CO oxidation on Pd/CeO_2 catalysts, *Angew. Chem. Int. Ed.* 134 (2022) e202200434, <https://doi.org/10.1002/ange.202200434>.
- [69] K. Chen, W. Li, Z. Zhou, Q. Huang, Y. Liu, Q. Duan, Hydroxyl groups attached to Co^{2+} on the surface of Co_3O_4 : a promising structure for propane catalytic oxidation, *Catal. Sci. Technol.* 10 (2020) 2573–2582, <https://doi.org/10.1039/dcyy00265h>.
- [70] Z. Zhao, G. Li, Y. Sun, N. Li, Z. Zhang, J. Cheng, C. Ma, Z. Hao, The positive effect of water on acetaldehyde oxidation depended on the reaction temperature and MnO_2 structure, *Appl. Catal. B: Environ.* 303 (2022) 120886, <https://doi.org/10.1016/j.apcatb.2021.120886>.